Subantarctic and Polar fronts of the Antarctic Circumpolar Current and Southern Ocean heat and freshwater content variability: A view from Argo*

Donata Giglio† and Gregory C. Johnson‡

*Joint Institute for Marine and Atmospheric Research Contribution No. 2477 and Pacific Marine Environmental Laboratory Contribution No. 4350

†*Corresponding author address:* Donata Giglio, Joint Institute for the Study of the Atmosphere and Ocean, University of Washington, Box 355672, Seattle, WA 98195.

E-mail: dgiglio@uw.edu

‡NOAA/Pacific Marine Environmental Laboratory, 7600 Sand Point Way NE Bldg. 3, Seattle, WA 98115.

ABSTRACT

Argo profiling floats initiated a revolution in observational physical oceanography by providing numerous, high-quality, global, year-round in situ ($0-2000$ dbar) temperature and salinity observations. Here, we use Argo's unprecedented sampling of the Southern Ocean during $2006-2013$ to describe the position of the Antarctic Circumpolar Current's Subantarctic and Polar fronts, comparing and contrasting two different methods for locating fronts using the same data set. The first method locates three fronts along dynamic height contours, each corresponding to a local maximum in vertically integrated shear. The second approach locates the fronts using specific features in the potential temperature field, following Orsi et al. (1995). Results from our analysis of Argo data are compared to those from Orsi et al. (1995) and other more recent studies. Argo spatial resolution is not adequate to resolve annual and interannual movements of the fronts on a circumpolar scale, since they are on the order of 1° latitude (Kim and Orsi 2014), smaller than the resolution of the gridded product analyzed. Here, Argo's four-dimensional coverage of the Southern Ocean equatorward of $\sim 60^\circ$S is used to quantify variations in heat and freshwater content there with respect to the time-mean front locations. These variations are described in the Southern Ocean and in regions between fronts during $2006-2013$, considering both pressure and potential density ranges (within different water masses) and relations to wind forcing (Ekman upwelling and downwelling).

1. Introduction

Over the last three decades, the Southern Hemisphere climate has experienced dramatic changes: growth of the Ozone Hole (Hofmann et al. (1997); WMO (2011); http://www.nature.com/nature/focus/ozonehole/), increased melting of the West Antarctic ice-sheet (Ding et al. 2011; Rignot et al. 2014), overall thinning of the Antarctic ice-schelf (Paolo et al. 2015), stronger winds (Marshall 2003; Thompson et al. 2011), and ocean warming (Gille 2008; Sutton and Roemmich 2011; Roemmich et al. 2015). The Southern Ocean warming and freshening of water masses (Böning et al. 2008; Johnson et al. 2008; Purkey and Johnson 2010; Meijers et al. 2011; Purkey and Johnson 2013) may be related to regional trends in sea ice extent (Holland and Kwok 2012) or ice sheet melt (Jacobs and Giulivi 2010), and may also drive ice sheet melting by ocean advection of heat (Rignot et al. 2013; Schmidtko et al. 2014; Alley et al. 2015). Because of its large heat capacity and influence on the Meridional Overturning Circulation (MOC), the Southern Ocean is not only key for heat and freshwater redistribution in the global climate system (Lumpkin and Speer 2007; Marshall and Speer 2012; Watson et al. 2014), but also for the global atmosphere-ocean carbon budget (Sabine 2004; Boutin et al. 2008; Le Quere et al. 2009; Ito et al. 2010; Sallee et al. 2012). A quarter of all anthropogenic CO_2 emissions have been captured in the Southern Ocean, with a main contribution by transformation of water masses within the Antarctic Circumpolar Current and their subsequent sinking below the surface (Sabine 2004; Ito et al. 2010).

The Antarctic Circumpolar Current (ACC), the world's largest current, is the main feature of the Southern Ocean and is dynamically connected with the MOC, which ventilates deep and bottom portions of the Pacific, Atlantic, and Indian oceans (Lumpkin and Speer 2007; Johnson 2008; Marshall and Speer 2012). Also, the ACC circulation blends together water masses formed in

different basins (Rintoul et al. 2001; Van Sebille et al. 2013). The ACC is not a smooth, large-scale flow. Rather, most of its transport is concentrated in a series of well-separated fronts (Orsi et al. 1995; Sallée et al. 2008; Sokolov and Rintoul 2009a,b; Thompson et al. 2010; Thompson and Sallee 2012; Kim and Orsi 2014). These features separate regions with distinct temperature and salinity signatures and are associated with deep-reaching jets and subduction or upwelling of different water masses. In a landmark paper, Orsi et al. (1995) (hereon OWN95) describe average properties of the fronts using station data from multiple synoptic transects. Three fronts are identified between the Southern Boundary of the ACC and the Subtropical Front to the north: the Southern ACC front, the Polar Front, and the Subantarctic Front. Initially the presence of multiple cores in these ACC fronts was not detected, given the coarse meridional spacing of station data, but has since been revealed (Sokolov and Rintoul 2002, 2007, 2009a; Anilkumar et al. 2006). Numerous regional analyses of the ACC frontal structure are based on in situ oceanographic profile or surface (i.e. surface drifter or satellite) data. Most common domains for these studies are in Drake Passage (Cunningham and Pavic 2007; Firing et al. 2011; Renault et al. 2011), around the Kerguelen Plateau (Sparrow et al. 1996; Belkin and Gordon 1996; Park et al. 2009, 2014; Tarakanov 2014), and along the ACC sector south of Australia and New Zealand (Belkin and Gordon 1996; Sokolov and Rintoul 2002; Budillon and Rintoul 2003; Sokolov and Rintoul 2007). Additional analyses have been carried out south of Africa (Belkin and Gordon 1996), and in the South Atlantic (Peterson and Whitworth 1989; Boehme et al. 2008; Billany et al. 2010), Indian (Belkin and Gordon 1996; Anilkumar et al. 2015), and Eastern Pacific (Tarakanov 2011) sectors of the Southern Ocean.

Beside hydrographic data (OWN95, Böning et al. (2008)), surface observations from satellites have been widely used to describe the ACC fronts on a global (circumpolar) scale (Gille 1994; Dong et al. 2006; Sallée et al. 2008; Sokolov and Rintoul 2009a,b; Thompson and Sallee 2012;

Kim and Orsi 2014). Sallée et al. (2008) and Sokolov and Rintoul (2009a,b) combine the mean dynamic topography from in situ profiles (referenced to 1500 and 2500 dbar respectively), with altimetry data to study both the time mean and variability of the fronts' location through a contour-based approach (Sokolov and Rintoul 2007, 2009a,b). The applicability of this method has been debated (Graham et al. 2012; Thompson and Sallee 2012; De Boer et al. 2013; Gille 2014). Graham et al. (2012) find that gradient maxima in the sea surface height field are the most reliable indicator of a front's location, while using sea surface height (SSH) contours can give misleading results for the temporal variability of the frontal position. Yet Chapman (2014) shows that the contour-based approach is more accurate than other methods (i.e. gradient, PDF and wavelet/HOS methods) at all signal to noise ratios, when applied to a synthetic SSH field. Finally, SSH anomalies of meandering jet-like features are associated with non-Gaussian probability density function (Thompson and Demirov 2006), allowing study of ACC fronts with altimetry observations (Shao et al. 2015). No estimates of the mean dynamic topography are required, ensuring that any temporal variability in frontal location is unaffected by large-scale SSH changes.

Kim and Orsi (2014) find large year-to-year meridional fluctuations in frontal locations in the southeast Pacific during $1992-2011$ using altimetry data and a contour-based approach (with a mean dynamic topography that combines GRACE and Argo observations). These fluctuations are related mostly to the El Niño-Southern Oscillation (ENSO) and in part to the Southern Annular Mode (SAM), with no apparent seasonal cycles or long-term trends detected in this region. In contrast, in the southeast Indian ocean fronts shift to the south in summer and to the north in winter. Also, a long-term southward drift of the ACC fronts is observed in the Indian sector. This movement is hypothesized to be a response to the poleward expansion of the Indian subtropical gyre. Gille (2014) finds no long-term trend in the zonally averaged ACC transport latitude index (i.e. based on the (zonal) transport-weighted average latitude) from altimetry data, a weak sensitivity

to the Southern Annular Mode, and no correlation with ENSO. Also, Gille (2014) suggests that the poleward trend in SSH contours might be associated with large-scale changes in SSH due to a warming ocean more than with localized shifts in frontal positions. Recently, Shao et al. (2015) also show that the ACC as a whole and on regional spatial scales does not exhibit significant meridional trends between 1993 and 2012, and is relatively insensitive to climate mode-induced variability except in the East Pacific (where they find correlation between the basin-averaged Subantarctic and Polar fronts' position and SAM, with a positive SAM corresponding to a northward shift) and south of Australia (with the Polar Front shifting southward during positive SAM).

Since the ACC fronts are linked to ocean dynamics (current strength), thermodynamics (sites of water mass transformation; OWN95), and the pattern of upwelling/downwelling associated with the closure of the global overturning circulation (Marshall and Speer 2012), the structure of the fronts is closely related to the distribution of heat and freshwater in the Southern Ocean. Analysis of in situ data shows how coherent warming and freshening trends in the Southern Hemisphere extend deeper than 1,000 m and are partially related to water mass changes within the ACC (Böning et al. 2008). Altimetry data, too, reveal similar changes in the ACC (Meijers et al. 2011), with diabatic processes contributing to cooling, while playing a key role in observed freshening. During $2006-2013$, in the upper 2000 dbar of the global ocean sampled by Argo floats, the Southern Hemisphere ocean is the main recipient of heat from global warming, with regional patterns indicating cooling south of 50°S in the Pacific (Roemmich et al. 2015). Multidecadal warming and/or freshening in the ACC is also reported (Aoki et al. 2005; Sprintall 2008; Naveira Garabato et al. 2009; Tarakanov 2011; Kobayashi et al. 2012; Schmidtko and Johnson 2012; Close et al. 2013; Yang and He 2014), with some exceptions related to regional dynamics, such as the influence of the Agulhas Rings south of Africa (Swart and Speich 2010).

Here we use Argo's unprecedented sampling of the Southern Ocean (Roemmich et al. 2015) during 2006−2013 to describe the position of the ACC Subantarctic and Polar fronts based on subsurface water properties. We detect fronts using two different methods, and compare with results from OWN95 and other more recent studies. Argo spatial resolution is not adequate to resolve annual and interannual movements of the fronts locally, since they are on the order of 1 degree latitude (Kim and Orsi 2014). Yet Argo four-dimensional coverage of the Southern Ocean equatorward of $\sim 60^{\circ}$S can be used to identify fronts and quantify heat and freshwater content variations in the Southern Ocean. Here, we describe changes in heat and freshwater content in the Southern Ocean (within the Argo domain) and regions in between the mean front locations during 2006−2013, considering both pressure and potential density ranges (different water masses) and relations to wind forcing (Ekman upwelling and downwelling).

We describe data and methods in Section 2. We find frontal locations using Argo data, comparing a Dynamic Height (DH) contour approach (Section 3a) with a potential temperature (θ) feature-based method (Section 3b). We relate these results from Argo to the findings of OWN95 and more recent studies and discuss the θ-S properties at the fronts (Section 3c). Also, we analyze changes in heat and freshwater content from 2006−2013 in the Southern Ocean (within the Argo domain) and for different regions in between fronts, discussing the relation between θ-S variability and wind forcing (Section 4). We summarize and conclude in Section 5.

2. Data and methods

a. Data.

Argo temperature and salinity profiles provide global in situ ($0-2000$ dbar) ocean observations, except on continental shelves, in marginal seas, and, until recently, seasonally ice-covered regions

(Klatt et al. 2007), with unprecedented sampling of the Southern Ocean (Roemmich et al. 2009). We use objectively mapped monthly fields (Roemmich and Gilson 2009) on a 1×1 degree grid from 64.5°S-64.5°N constructed from Argo temperature and salinity observations during $2006-2013$, after quality control and adjustment of pressure bias. In order to test how the mapping may affect the analysis in lightly sampled regions, we check that the resulting frontal locations are consistent with the original profile data (see Supplemental material).

b. Methods to locate the fronts.

ACC fronts are associated with strong gradients in temperature and salinity, and with deep-reaching jets (OWN95). Here, we compare two methods to identify the Subantarctic and Polar fronts of the ACC in a gridded Argo product. The first approach locates fronts along Dynamic Height (DH) contours that correspond to local maxima in vertically integrated shear (Section 2b.1). The second approach follows the fronts along specific features in the potential temperature field (Section 2b.2), similarly to OWN95. Results (Section 3) show the locations of the fronts as probability of occurrence (Figs. 3, 4) and time-averaged during $2006-2013$ (Figs. 2b, 5, 6, 10), once the annual variability is removed from the Argo fields (annual displacements of the fronts are not resolved by Argo). The DH and feature-based methods are in overall good agreement with each other, and only the DH approach is used in the second part of the manuscript.

1) FRONTS ALONG DYNAMIC HEIGHT CONTOUR LINES.

Fronts are characterized by strong geostrophic currents. To find those DH contours that are aligned with fronts, we consider a set of DH bins and count (for each) the number (N, monthly) of co-located local maxima in $0-1975$ dbar integrated shear (within the Argo domain in the Southern Ocean), i.e. local maxima in geostrophic velocity amplitude at the surface from DH referenced

to 1975 dbar. The sum of N (in time) is characterized by three peaks, each identifying a different DH range (Fig. 1). Each DH range is associated with a different front (e.g. front i), and a contour (DH_i^*) within that range is assigned to the front (red lines in Fig. 1). DH_i^* is the time average DH of DH bins (within range i) that correspond to monthly local peaks in N. Thus front i is described using $\mathrm{DH}_i^* = \overline{\mathrm{DH}_{\mathrm{N}_{i_{\max}}}(t)}$, where $\mathrm{DH}_{\mathrm{N}_{i_{\max}}}$ is associated with the maximum N within the DH range i (i.e. $\mathrm{N}_{i_{\max}}$) for a given month t. The standard error of DH_i^* is related to the time variability of the DH bin that corresponds to $\mathrm{N}_{i_{\max}}$ (i.e. $\mathrm{DH}_{\mathrm{N}_{i_{\max}}}$), and is small (Fig. 1). Finally, the DH bin size in Fig. 1 is .5 $\mathrm{m}^2\mathrm{s}^{-2}$. Varying this dimension between .15 and .7 $\mathrm{m}^2\mathrm{s}^{-2}$ yields DH^* values that are generally comparable to one another within errorbars.

Based on their position and θ-S properties, the three fronts identified here are named, from north to south (i.e. decreasing values of DH contours): Northern Subantarctic front (nSAf), Southern Subantarctic front (sSAf), and Polar front (Pf). These names do not necessarily correspond to those in other studies that describe a different number of cores for each ACC front (e.g. Sokolov and Rintoul (2002, 2007, 2009a); Anilkumar et al. (2006)). The spatial scales of the gridded Argo product are larger than available altimetry products and cannot resolve all the cores of the ACC fronts. Also, Argo data still undersample the southern fronts of the ACC, where seasonal sea ice was once a hurdle for deployments (Klatt et al. 2007).

2) Fronts along specific features of the potential temperature field.

Based on the description by OWN95 (their Table 3) and consistent with subduction and/or shoaling of water masses, we locate fronts in the Argo dataset along characteristic θ features (Table 1). That is, we locate a front at the intersection between a constant θ^* surface and (for the SAf) a pressure level or (for the Pf) a θ-extremum surface (e.g. the maximum θ deeper than 800 dbar). We compare frontal locations by OWN95 with those estimated from Argo data using θ^* values

consistent with OWN95 (see θ^* values in Table 1 and resulting frontal locations later in Fig. 5). OWN95 do not describe two branches of the Subantarctic Front, but provide a θ range (at 400 dbar) to characterize it: we associate the minimum and maximum values of this θ range with the sSAf and nSAf respectively. Also, we compute (Table 1) θ^* values along the frontal locations from the DH contour approach (i.e. the circumpolar and time average of θ at the x, y intersection between the DH^*_i contour associated with front i and the pressure level or θ-extremum surface of interest), and compare the two (DH- versus θ-based) methods (Fig. 6). This procedure for local comparisons is motivated by the possibility of using a θ-contour as boundary between water masses (OWN95) and by an overall circumpolar agreement between the DH- versus θ- (i.e. water mass-) based approach. Such agreement is seen in how the average θ profiles along the DH-based Pf, sSAf, and nSAf separate regions where the water-mass volumes in the Southern Ocean (within the Argo domain) peak (Fig. 2a), i.e. where θ values are fairly homogeneous and characteristic of that region and pressure level (regions at the boundary of the domain are not well represented in Fig. 2a). These peaks, although sometimes weak (e.g. between the sSAf and the nSAf), have a coherent structure in the p-θ_{bin} plane, consistent with a circumpolar frontal structure of the ACC that can be described using θ-criteria (OWN95). Yet the peaks are not observed at all individual longitudes, partially due to the resolution of the data (especially where different fronts are close to one another) and the limited southward extent of the Argo domain.

We evaluate a set of θ features or criteria for each front (see Table 1 and Supplemental material; in this manuscript, the word "criteria" is used in the context of the θ-method to locate the fronts, which is based on, but does not strictly follow, the characterization in OWN95). Here we focus on those criteria that align best with results from the DH contour method, i.e. yield the best overall agreement both in circumpolar location, and θ-S properties at different pressure levels. These features (Table 1, in bold) are identified by θ^* values of the maximum θ (hereon max(θ)) deeper

than 800 dbar (to locate the Pf), and of θ at 400 dbar (to locate the sSAf and the nSAf). For the Pf, the max(θ) criterion at p$\geq$ 800 dbar does not strictly follow the characterization in OWN95. OWN95 describe the Polar Front as being south of where $\theta_{max} > 2.2$°C at p$\geq$800 dbar (their Table 3), with θ_{max} a local vertical maximum. In the Argo dataset, this θ_{max} is generally shallower than 800-850 dbar (not shown), hence the max(θ) at p$\geq$800 dbar criterion (Table 1) captures θ_{max} only at some longitudes, and constrains θ at 800 dbar elsewhere (since max(θ) is the largest value of θ in a pressure range and not necessarily a local vertical maximum).

The θ_{max} at depth is related to a θ_{min} (i.e. θ local vertical minimum) in the upper ocean, which has been used to characterize the Polar front (OWN95), and is described here as an alternate θ criterion, although it does not align with the DH-based Pf as well as an isotherm along the max(θ) at p$\geq$800 dbar does. This θ_{min} is present only during summer. Hence, with year-round data from Argo, we favor the deeper criteria in this analysis. Also, the θ_{min} is generally shallower than 200 dbar (not shown), hence the minimum θ (hereon min(θ)) at p$\leq$200 dbar criterion we use (Table 1) is equivalent to the characterization in OWN95 (their Table 3), except that it includes profiles where the θ_{min} is not present (e.g., winter-time profiles; common in Argo data, but not previous hydrographic data). We discuss other θ and S features along the fronts and how they align with the DH-based approach in the Supplemental material.

c. Freshwater estimate from Argo salinity anomaly.

Freshwater anomalies (FW) for a region of interest, are estimated as centimeters of freshwater over the area of the Southern Ocean in the gridded Argo domain ($A_{SO} = 6.001 \cdot 10^{13} m^2$), i.e. FW=$V_{FW}/A_{SO}$. The freshwater volume, V_{FW}, is defined as the amount of freshwater that would need to be added to or removed from a reference volume V_m (with salinity S_m), in order to obtain salinity S_i (at timestep i), without modifying the salt content of the water, i.e.

$V_{FW} = \int \left(\frac{S_m}{S_i} - 1 \right) dV_m$. Here, V_m is the volume associated with the Argo grid in the region and pressure levels of interest, and S_m and S_i are the corresponding time mean and time changing salinity.

3. The Polar and Subantarctic fronts of the ACC from Argo

a. Fronts along dynamic height contour lines.

The location of the Pf cannot be determined everywhere in the Pacific sector of the Southern Ocean, since, at some longitudes, the Pf is poleward of the Argo domain and the gridded maps. The Argo Pf shows good agreement with (i.e. only slight differences from) OWN95's estimate in Drake Passage (Fig. 3, red #1), between the Maurice Ewing Bank (Fig. 3, red #2) and the Atlantic Ridge (Fig. 3, red #4), between $150-170°$E and $175-120°$W in the Pacific, and between $35-55°$E and $100-115°$E in the Indian sector (Fig. 3). In other regions, the Argo Pf is further south than the previous estimate of OWN95 and is more consistent with the middle branch of the Polar Front in Sokolov and Rintoul (2009a) which generally agrees well with our Argo Pf circumpolar location. We observe a large southward shift in the Argo Pf position relative to OWN95 at the Maurice Ewing Bank (Fig. 3, red #2; consistent with Sokolov and Rintoul (2009a) and Kim and Orsi (2014)), in the eastern Atlantic and between $115-145°$E (consistent with Sokolov and Rintoul (2009a) and different from Kim and Orsi (2014)), and around the Kerguelen Plateau (Fig. 3, red #6), with the Argo Pf flowing just north of the Fawn Trough (Fig. 3, red #7). In this region, our results are consistent with Sparrow et al. (1996) and Sokolov and Rintoul (2009a), but neither Kim and Orsi (2014) nor Park et al. (2014) (discussed further in Section 3b).

We find two cores of the Subantarctic Front in the Argo dataset, the sSAf and the nSAf. Along most of their circumpolar path, these two cores are consistent with the southern and middle branch

of the Subantarctic Front in Sokolov and Rintoul (2009a), respectively, with the largest differences in the Pacific Ocean, east of the Campbell Plateau (Fig. 3, red #9). Here, the nSAf sharply veers northward to follow the bathymetry and comes back to the south around 180°E, consistent with the Subantarctic Front in Böning et al. (2008) and Kim and Orsi (2014), and with the northern (rather than the middle) branch of the Subantarctic Front in Sokolov and Rintoul (2009a). Similarly, the nSAf sharply veers northward at the East Pacific Rise (Fig. 3, red #14), again in agreement with Böning et al. (2008) and the northern (rather than the middle) branch of the Subantarctic Front in Sokolov and Rintoul (2009a), but not Kim and Orsi (2014), where no sharp northward meandering is observed. In general, the Argo sSAf traces more closely (than the nSAf) the location of the Subantarctic Front in OWN95, except in the western Atlantic (near South America), in the Indian Ocean eastward of 70°E, and in the eastern Pacific. Also, in OWN95, both the Subantarctic and Polar fronts cross the Pacific-Antarctic Ridge via the Udinsev Fracture Zone (Fig. 3, red #11). Results here suggest that only the Pf does (Fig. 3, red #11), in agreement with Kim and Orsi (2014) and Sokolov and Rintoul (2009a), while the sSAf goes through the Eltanin Fracture Zone (Fig. 3, red #12) and the nSAf through the Menard Fracture Zone (Fig. 3, red #13). However, the Argo climatology resolution may be a limitation when describing the front position in relation to these narrow bathymetric features.

The location of the ACC fronts from Argo agrees well with local maxima of the zonal and meridional baroclinic geostrophic transport in the upper 1975 dbar from Argo (Fig. 4, with velocities referenced to 1975 dbar). Such agreement is expected on the overall circumpolar scale (since DH_i^* contour values are chosen based on Argo integrated shear on a circumpolar scale, Section 2b.1) and Fig. 4 shows that it holds also locally. As an example, the northward meandering of the nSAf east of the Campbell Plateau (Fig. 3, red #9) and at the East Pacific Rise (Fig. 3, red #14) aligns

with a pattern of stronger meridional velocities (Fig. 4b). The strongest integrated transport is in the western Indian ocean, associated with the Agulhas retroflection (Fig. 4a).

b. Fronts along specific features of the potential temperature field.

The Pf location using θ^* values by OWN95 in the Argo θ field (Section 2b.2) is in overall agreement with OWN95, but regional discrepancies between the shallower and deeper criterion are large between $50-80°$E, $\sim 115-140°$E, and $\sim 170-150°$W (Fig. 5). Around the Kerguelen Plateau (i.e. $50-80°$E), a Pf criterion on the $\max(\theta)$ deeper than 800 dbar yields a path of the Pf that is south compared to the upper ocean $\min(\theta)$ criterion (Fig. 5), except for some of the individual Argo profiles that align with the shallower criterion between $70-80°$E (Fig. S1c in the Supplemental material). These profiles do not fall on a circumpolar path (Fig. S1c), and the corresponding θ field yields large errorbars for the Pf from the $\max(\theta)$-criterion in Fig. 5 (between $70-80°$E). In summary, the shallower criterion suggests a Pf location (in the region of interest) that is to the north compared to following θ^* along $\max(\theta)$ deeper than 800 dbar. The shallower criterion is based on a θ_{min} (OWN95) that is present only during summer. With year-round data from Argo, we favor the deeper criteria in this analysis.

Using 2°C as the θ^* value for the $\min(\theta)$-based Pf (as in Fig. 5) is consistent with Table 3 in OWN95 and is similar to the criterion in Park et al. (2014) (who consider θ_{min} in the $100-300$ m depth range), but the resulting front location is different from both of the other studies. In the gridded Argo product used here, the 2°C contour of the minimum θ in the upper 200 dbar (i.e. a $\min(\theta)$-based Pf) sharply veers northward at the plateau (65°E, Fig. 5), while in OWN95 their Polar Front gently veers northward between 55 and $\sim 62.5°$E (Fig. 5), and in Park et al. (2014), the 2°C isotherm that corresponds to their Polar Front veers northward around 71°E (their Fig. 5).

A northward change in direction, west of 70°E, as in the gridded Argo product here, is consistent with individual Argo profile observations (see Supplemental material).

The sSAf and the nSAf locations using θ^* values by OWN95 in the Argo θ field (Section 2b.2) align with the Subantarctic Front in OWN95 only in few sectors of the ACC (e.g. around 110°E, Fig. 5). At other longitudes, one of them may be close to the previous estimate but not the other (e.g. the sSAf around 175°W) or they are both far (generally to the north, e.g. in the Atlantic basin). Sectors of the Southern Ocean where Argo fronts based on θ^* values in OWN95 are equatorward of the position in OWN95 indicate that the regional Argo climatology at the pressure levels of interest (for the criteria) is colder than previous observations (collected between $1976-1990$ for sections in the Atlantic Ocean, and $1974-1977$ in the western Indian basin). Unfortunately, a regional long term trend cannot be estimated due to the sparsity of observations in the Southern Ocean for the period previous to Argo. The simple comparison (here) of the Argo versus OWN95 frontal locations may be aliased by interannual and decadal variability, as well as by differences between the two datasets (temporally and spatially distributed Argo profiles versus synoptic, mostly summertime sections) and methods. Yet Argo profile data (with no annual cycle removed, Fig. S1b) that follow the 2°C shallow criterion lay north of the Polar Front location in OWN95 in the same ACC sectors ($140-170$°E and 175°E-120°W) as for the gridded data (with the annual cycle removed, Fig. 5). Also, ECMWF ERA-Interim Sea Surface Temperature (SST) shows a statistically significant linear decrease between 1979 and 2013 in the general ACC Pf region at those longitudes (not shown), consistent with a local long term cooling of the upper ocean and with the min(θ)-based Argo Pf being equatorward of the Polar Front in OWN95. Regional cooling is not inconsistent with the overall warming of the Southern Ocean observed for the last few decades and during the Argo period (Roemmich et al. 2015).

We compute θ^* values (analogous to those of OWN95) along DH contours that identify fronts as in Section 2b.1 (Table 1). Resulting frontal locations are in overall good agreement with the DH contour approach (Fig. 6), showing how the two methods, described in Section 2b.1 and 2b.2, align regionally (the agreement on a circumpolar scale is discussed in Section 2b.2).

Also, the θ^* value of the upper ocean $\min(\theta)$ computed along the DH-based Argo Pf, agrees, within errorbars, with the value in Sokolov and Rintoul (2009a), but not OWN95 (Table 1). However, the value of the $\max(\theta)$ at p$\geq$800 dbar along the DH-based Argo Pf agrees with both the previous findings, as does θ(400 dbar) along the DH-based Argo nSAf (Table 1). In contrast, along the DH-based Argo sSAf, θ(400 dbar) differs from both OWN95 and Sokolov and Rintoul (2009a) (Table 1). A main advantage in computing θ^* values along DH- (i.e. streamline-) based fronts here resides in having both the streamfunction and the θ field from the same well-resolved (Argo) dataset and for the same time period ($2006-2013$).

Argo fronts from θ criteria that generally agree best with the DH contour method (in bold in Table 1, with θ^* values computed along DH-based fronts), still fail to align with it in a few regions (Fig. 6), suggesting that, in specific sectors of the Southern Ocean, a combination of different criteria (Table 1 and Supplemental material) may be appropriate to locate the fronts more accurately when using a feature-based approach. In the eastern Pacific, the nSAf (from θ) hits the South American coast, rather than flowing through Drake passage. This may be related to how formation of Subantarctic Mode Water impacts the θ-field in the region and can be corrected using a regional criterion on θ at $600-$dbar (see Supplemental material). Around 90°E, the θ-based sSAf and nSAf flow south of the corresponding DH-fronts (a $600-$dbar criterion for θ would reduce this departure too). In the Atlantic basin, the sSAf and nSAf flow north of the DH-fronts (reduced applying a salinity criterion in the region).

c. θ-S properties along the fronts: time mean and interannual variability.

Time-mean θ-S diagrams along the Pf and the nSAf are similar using the DH contour method versus θ criteria with θ^* values by OWN95 (Fig. 7a). However, the sSAf from the latter shows θ-S properties in between the DH-based sSAf and nSAf (Fig. 7a).

The Pf θ-S diagram from Argo shows a θ minimum (θ_{min}) in the upper 200 dbar and a θ maximum (θ_{max}) at depth (Fig. 7b), as described in OWN95. However, the θ_{min} is colder than 2°C, and the θ_{max} is between $400-700$ dbar, consistent with the description in Section 3b.

The θ^* values computed along the DH frontal locations yield fronts with θ-S properties that agree well with the DH method (Fig. 7b). While this result is expected at the pressure level of interest for the θ-criteria (since θ^* values are computed along DH-fronts), the overall agreement of the θ-S curves is further evidence of how the two methods, described in Section 2b.1 and 2b.2, are consistent with appropriate θ^* choices. Also, the difference in salinity arising from using one approach versus the other for the SAf is consistent with the observed northward departures of the θ-based sSAf and nSAf in the Atlantic compared to the DH-approach (Fig. 6), and could be reduced by including a regional salinity criterion. Results in the rest of the manuscript are based on the DH contour method.

θ-S properties of the Argo nSAf and Pf show interannual variability during $2006-2013$ (Fig. 8). Deeper than 200 dbar, the nSAf was warmer and saltier in 2008 compared to 2011 (Fig. 8a), while the Pf was colder and fresher in $2006-2009$ compared to $2011-2013$ (Fig. 8b). At these pressure levels, changes in θ and S are mostly compensating in density. This is not the case for the Pf θ_{min} in the upper 200 dbar, where θ-S properties were colder and saltier in $2006-2007$ compared to $2010-2011$ (Fig. 8b). Since the θ-S properties of interest are along a fixed DH contour, θ-S anomalies must compensate in density in a vertically integrated sense.

4. Heat and freshwater content in the Southern Ocean

We describe changes in heat and freshwater content in different regions around the ACC. We define these regions (within the Argo domain) based on the time mean location of the Polar, Subantarctic, and Subtropical fronts (Section 3a; Fig. 2b). The SO region extends south of the STf, n.nSAf is between the STf and the nSAf, SAf.nPf extends from the nSAf to the north of the Pf, and Pf.s includes the Pf and south of it. The Subtropical front (STf) is used as our northernmost boundary, and is located along the 12°C isotherm at 100 dbar (OWN95). Due to the time-constant boundary for each region, frontal shifts may influence θ-S changes locally within the region. Yet the effect on resulting circumpolar heat and freshwater anomalies may be small (e.g. meridional displacements may be to the south at some longitudes and to the north at others (Shao et al. 2015)). Also, interannual variability in frontal locations may not be large enough to be detected robustly in Argo.

We describe interannual variability of heat and freshwater content in pressure ranges and density classes (water masses) in Section 4a, and related θ-S anomalies in Section 4b. In Section 4c, we discuss how wind-forced vertical advection (i.e. Ekman downwelling) causes isopycnals to deepen in $2010-2012$, contributing to the observed ocean warming signal.

a. Heat and freshwater content interannual variability.

The SO heat content (in the upper 1975 dbar) increased during $2006-2013$ (Roemmich et al. (2015) and Fig. 9a) with contributions from all three of the regions considered here, and especially n.nSAf (red line, Fig. 9a). Most of this increase is confined to the top 1000 dbar (Fig. 9c,e), with weaker signal between $1000-1500$ dbar (Fig. 9g) and a positive anomaly in 2006 for the Pf.s region between $1500-1975$ dbar (Fig. 9i, blue line). At these pressure levels the SO anomaly

in 2006 and 2007 is smaller than the related standard error, while the n.nSAf heat content is characterized by negative anomalies in 2006 – 2009 and positive later, as in shallower layers.

The SO freshwater anomaly in the upper 1975 dbar (computed as in Section 2c) is negative in 2009 and 2013, and positive in 2011−2012, with different contributions from different regions (Fig. 9b). In n.nSAf, the FW anomaly is positive in 2006 – 2007 and 2011, and negative in 2012 – 2013, as a nearly linear decrease that dominates the SO signal in the upper 500 dbar (Fig. 9d, red line) is added to increasing freshwater between 1000 – 1975 dbar (Fig. 9h,j), with the transition occurring between 500 – 1000dbar (Fig. 9f). The SAf.nPf region too has different phasing between the upper 500 dbar and the deeper levels, with a contribution to the SO signal that is small in the shallowest layer, and larger at depth. Finally, Pf.s provides the smallest contribution to the FW interannual variability in the SO, with the exception of the 2011 positive and 2013 negative anomalies (Fig. 9b, blue line), that are related to changes in shallower (Fig. 9d) and deeper (Fig. 9f,h,j) layers, respectively. The yearly freshwater anomaly (in the upper 1975 dbar, Fig. 9b) varies spatially in each region (Fig. 10). The 2006 – 2007 positive anomaly (Fig. 9b) is dominated by variability in the Indian sector of n.nSAf, south of the nSAf in the central South Pacific, and south of the STf in the South Atlantic (especially in 2007) (Fig. 10a-b). However, the 2011 – 2012 positive anomaly (Fig. 9b) is set by variability south of the nSAf in the South Indian ocean, in n.nSAf and SAf.nPf in the central and eastern South Pacific and western (and eastern, in 2012) South Atlantic, and in the Pf.s region (in 2011) (Fig. 10f-g). The 2009 negative anomaly (Fig. 9b) is dominated by the signal south of the nSAf in the South Indian ocean, south of the STf in the central and eastern South Pacific and western South Atlantic, and in n.nSAf and SAf.nPf in the eastern South Atlantic (Fig. 10d). Finally, the 2013 negative anomaly (Fig. 9b) is set by the signal in the Indian sector of n.nSAf, south of the STf in the western and central South Pacific, and south of the Pf in the central and eastern Atlantic and in the western Indian Ocean (Fig. 10h).

Overall warming during $2006-2013$ is also observed for water masses in the potential density (σ_θ) range $26.8 \leq \sigma_\theta \leq 27.7$ kg m^{-3} (Fig. 11, top panels), with a stronger signal for Subantarctic Mode Water ($26.8 \leq \sigma_\theta \leq 27.0$ kg m^{-3}). FW anomalies indicate freshening of water masses for $27 \leq \sigma_\theta \leq 27.45$ kg m^{-3} (Fig. 11e), with positive anomalies also in $2006-2007$ for $\sigma_\theta > 27.45$ kg m^{-3}. Also, the n.nSAf contribution to the SO signal for $\sigma_\theta > 27.0$ kg m^{-3} is a FW increase during the Argo years, at all levels. In contrast, in the SAf.nPf and Pf.s regions, for $\sigma_\theta > 27.35$ kg m^{-3}, water masses are characterized by a positive FW anomaly in 2006, 2007 (for SAf.nPf), and $2011-2012$ (Fig. 11g-h).

Finally, the FW anomaly in the SAMW range $26.8 \leq \sigma_\theta \leq 26.9$ kg m^{-3} is negative at the end of the time series and positive before that (Fig. 11e-f).

b. θ-S property changes on isopycnals.

Heat and freshwater changes in potential density classes described here (Fig. 11), are based on mean isopycnal locations. Yet θ-S properties vary differently on the actual time-changing isopycnals (Fig. 12 versus Fig. 13), with potential density decreasing in time on the mean isopycnal location (Fig. 12i-l). The θ-S anomalies in Fig. 12a-h are not scaled by layer thickness, but are consistent with heat and freshwater changes in Fig. 11, i.e. overall θ increase (Fig. 12a-d) and S decrease (Fig. 12e-h) during $2006-2013$, on most layers (except for salinity in the SAMW range). On the actual isopycnal locations θ increases in time at all levels, only in the SAf.nPf and Pf.s regions (Fig. 13c-d), and decreases for $\sigma_\theta < 27.3$ kg m^{-3} in the SO and n.nSAf (Fig. 13a-b). Also, in SAf.nPf and Pf.s, salinity increases (rather than decreases) on most isopycnals (Fig. 13g-h), while, in the SO, it does so only for $\sigma_\theta > 27.3$ kg m^{-3} (Fig. 13e). We find no significant salinity changes at such densities in n.nSAf (Fig. 13f).

c. Ekman upwelling and downwelling, and pressure changes on isopycnals.

We find an overall pressure increase on isopycnals in the Southern Ocean (Fig. 13i-l). In the SO, n.nSAf and SAf.nPf regions, Argo pressure changes are consistent with a contribution from wind-forced vertical advection (i.e. Ekman upwelling and downwelling, Fig. 14), estimated from ECMWF ERA-Interim zonal and meridional momentum flux at the ocean-atmosphere interface. The agreement holds only in $2007-2010$ in n.nSAf and it breaks down in Pf.s (not shown), where isopycnals shown in Fig. 14 (i.e. within the Southern Ocean Argo domain at each timestep) are shallower and direct heat and freshwater exchanges with the atmosphere play a greater role than dynamics. In Pf.s, isopycnals are also steeper and carry ventilation to great depths. In general, when comparing between Argo pressure changes on isopycnals and wind forcing, diabatic contributions are not the only mechanism at play besides vertical advection (e.g. lateral motion of sloping isopycnals may also affect how pressure on isopycnals changes over time). These additional processes may explain some of the differences in pressure changes on isopycnals between Argo and the estimate from ECMWF ERA-Interim (i.e. sign and/or amplitude differences in Fig. 14), along with the uncertainty on the Ekman upwelling and downwelling from reanalysis and on the Argo fields (e.g. in 2006, the number of Argo floats in the SO is smaller than in later years). The analysis of the relative contribution of heave and water mass processes to θ-S property changes (Durack and Wijffels 2010) would be a valuable (future) addition to this work, but is beyond the scope of the present study.

5. Summary and conclusions

We use Argo's unprecedented (e.g. spatially distributed with no bias towards summer months) sampling of the Southern Ocean during $2006-2013$ to describe the recent positions of the Antarctic Circumpolar Current's Subantarctic and Polar fronts equatorward of $\sim 60^{\circ}$S. We compare and

contrast two different methods for locating fronts in the same data set. The first method (Section 2b.1) locates three fronts along dynamic height contours, each corresponding to a local maximum in vertically integrated shear (Fig. 1). We term these the Polar front (Pf), Southern (sSAf) and Northern (nSAf) Subantarctic front (from south to north, Fig. 3). The second approach (Section 2b.2) locates the same fronts using specific features in the potential temperature field, consistent with subduction and/or shoaling of water masses (Table 1), following OWN95. The ACC fronts are associated with strong gradients in temperature and salinity, and with deep-reaching jets (OWN95), hence the two methods are in overall good agreement with each other. Argo DH-frontal locations align well both with local maxima of the zonal and meridional geostrophic transport in the upper 1975 dbar (Fig. 4), and with θ properties that separate regions where the Southern Ocean water mass volume (within the Argo domain) peaks (Fig. 2), i.e. regions with homogeneous θ properties. A local maximum in volume between the Pf and the sSAf is observed around 800 dbar and deeper (Fig. 2) and corresponds to the Upper Circumpolar Deep Water. Another maximum is located between the sSAf and the nSAf, at depths shallower than 1000 dbar (Fig. 2), and aligns with the freshest variety of Antarctic Intermediate Waters that begin to descend north of the Pf (not shown). The agreement between the two methods to locate the fronts also holds locally in most sectors of the Southern Ocean (Fig. 6), and for TS properties along the front (Fig. 7b). Yet the DH-approach is preferable since DH is a vertically integrated quantity, hence not as affected by local phenomena as θ at a specific pressure level (e.g. SAMW formation in the eastern Pacific Ocean). Phenomenological (θ-based) characterizations that align best with the DH fronts follow an isotherm of the max(θ) at p$\geq$800 dbar and of θ at p= 400 dbar, for the Pf and SAf (sSAf and nSAf), respectively, and are still not consistent with the DH approach in a few regions, i.e. the eastern Pacific for the nSAf, and around 90°E and in the Atlantic basin for the sSAf and nSAf. In these sectors of the Southern Ocean, the combination of different θ-S criteria may be appropriate

to locate the fronts more accurately. Also, the circumpolar θ^* value (of the isotherm at p= 400 dbar) that aligns best with the DH-based sSAf is different from previous studies (Table 1). A main advantage in computing θ^* values along DH- (i.e. streamline-) based fronts here resides in having both the streamfunction and the θ field from the same well-resolved (Argo) dataset and for the same time period ($2006-2013$). Argo frontal locations are consistent overall with findings in Sokolov and Rintoul (2009a), but show local differences with that study, OWN95, and other more recent analyses (Section 2b.1, e.g. at the Kerguelen and Campbell plateaus, the Maurice Ewing Bank, and crossing the East Pacific Rise). Our results focus on the time mean frontal locations. As for movements of the fronts in time, both a DH- and a θ- (contour) based method would be biased by θ variability in the Southern Ocean (Graham et al. 2012; Thompson and Sallee 2012; De Boer et al. 2013; Gille 2014). Large-scale changes in DH and θ contours may, in fact, be due to a warming ocean more than localized shifts in frontal positions. Also, Argo resolution may not be appropriate to detect such changes. The method described recently by Shao et al. (2015) based on altimetry anomalies, can be advantageous to track frontal movements in time.

We use Argo four-dimensional coverage of the Southern Ocean equatorward of $\sim 60^{\circ}$S to describe changes in heat and freshwater content in the Southern Ocean during $2006-2013$ with respect to the time-mean frontal location (Section 4). Heat content increases from $2006-2013$, in the upper 2000 dbar of the SO (i.e. south of the STf and within the Argo domain), with a signal that is mostly confined to the top 1000 dbar, and is weaker between 1000 and 1500 dbar. The FW anomaly (from the mean) in the top 2000 dbar of the SO is negative in 2009 and 2013, and positive in $2011-2012$, with a decrease during the time period of interest in the upper 500 dbar of the n.nSAf region (dominating the SO signal at those pressures), and an increase below 1000 dbar. Also, the yearly freshwater anomaly (in the upper 1975 dbar, Fig. 9b) varies spatially in each region considered here (Fig.10).

An overall increase of heat and freshwater content is observed for water masses in the range $26.8 \leq \sigma_\theta \leq 27.7$ kg m^{-3} (except for the STMW with $26.8 \leq \sigma_\theta \leq 26.9$ kg m^{-3}, where the FW anomaly is negative at the end of the time series, and positive earlier), with positive (SO) FW anomalies also in 2006−2007 for $\sigma_\theta > 27.45$ kg m^{-3} (Fig. 11). This heat and FW estimate in potential density classes (i.e., for water masses) is based on the mean isopycnal location. Yet θ-S properties vary differently on the actual time changing isopycnals (Fig. 12 versus Fig. 13), with anomalies that are opposite in sign (compared to values on the time-mean isopycnal location) for θ and S in the lighter and denser layers, respectively. This result suggests that heat and freshwater changes from using the mean isopycnal location may be partially related to isopycnal displacement.

We observe an overall pressure increase (in time) on isopycnals (Fig. 13i-l) consistent with wind-forced vertical advection by Ekman upwelling and downwelling (Fig. 14) in the SO, n.nSAf and SAf.nPf regions. Such wind-forced vertical advection causes isopycnals to deepen in $2010-2012$, contributing to the observed ocean warming signal.

Finally, ECMWF ERA-Interim SST shows a statistically significant linear decrease between 1979 and 2013 in the general ACC Pf regions at $140-170$°E and 175°E−120°W (not shown), consistent with a long term local cooling of the upper ocean and with the min(θ)-based Argo Pf (with the θ^* value by OWN95) being equatorward of the Polar front in OWN95 (Fig. 5), in these sectors of the Southern Ocean.

Acknowledgments. The Argo data used here were collected and are made freely available by the International Argo Program and by the national programs that contribute to it. The efforts of many international partners in planning and implementing the Argo array are gratefully acknowledged. ECMWF ERA-Interim SST data used in this study have been obtained from the ECMWF

Data Server. The objectively mapped Argo data were provided by John Gilson. DG was supported through a postdoctoral fellowship by the Joint Institute for the Study of the Atmosphere and Ocean (JISAO) under NOAA Cooperative Agreement NA15OAR4320063, Contribution No. 2477. GCJ is supported by NOAA Research and the NOAA Climate Observations Division. The statements, findings, conclusions, and recommendations herein are those of the authors and do not necessarily reflect the views of the National Oceanic and Atmospheric Administration or the Department of Commerce. Thanks to David Ferreira (U. Reading) and Matthew R. Mazloff (SIO) for the discussion about this work. Thanks to the two anonymous reviewers for providing valuable feedback.

References

Alley, R. B., S. Anandakrishnan, K. Christianson, H. J. Horgan, A. Muto, B. R. Parizek, D. Pollard, and R. T. Walker, 2015: Oceanic Forcing of Ice-Sheet Retreat: West Antarctica and More. *Annual Review of Earth and Planetary Sciences*, **43**, 207–231, doi:10.1146/annurev-earth-060614-105344.

Anilkumar, N., J. George, R. Chacko, N. Nuncio, and P. Sabu, 2015: Variability of fronts, fresh water input and chlorophyll in the Indian Ocean sector of the Southern Ocean. *New Zealand Journal of Marine and Freshwater Research*, **49**, 20–40, doi:10.1080/00288330.2014.924972.

Anilkumar, N., and Coauthors, 2006: Fronts, water masses and heat content variability in the Western Indian sector of the Southern Ocean during austral summer 2004. *Journal of Marine Systems*, **63**, 20–34, doi:10.1016/j.jmarsys.2006.04.009.

Aoki, S., N. L. Bindoff, and J. a. Church, 2005: Interdecadal water mass changes in the Southern Ocean between 30E and 160E. *Geophysical Research Letters*, **32**, L07 607, doi:

10.1029/2004GL022220.

Belkin, I. M., and A. L. Gordon, 1996: Southern Ocean fronts from the Greenwich meridian to Tasmania. *Journal of Geophysical Research*, **101**, 3675–3696, doi:10.1029/95JC02750.

Billany, W., S. Swart, J. Hermes, and C. J. C. Reason, 2010: Variability of the Southern Ocean fronts at the Greenwich Meridian. *Journal of Marine Systems*, **82**, 304–310, doi: 10.1016/j.jmarsys.2010.06.005.

Boehme, L., M. P. Meredith, S. E. Thorpe, M. Biuw, and M. Fedak, 2008: Antarctic Circumpolar Current frontal system in the South Atlantic: Monitoring using merged Argo and animal-borne sensor data. *Journal of Geophysical Research: Oceans*, **113**, C09 012, doi: 10.1029/2007JC004647.

Böning, C. W., A. Dispert, M. Visbeck, S. R. Rintoul, and F. U. Schwarzkopf, 2008: The response of the Antarctic Circumpolar Current to recent climate change. *Nature Geoscience*, **1**, 864 – 869, doi:10.1038/ngeo362.

Boutin, J., L. Merlivat, C. Hénocq, N. Martin, and J. B. Sallée, 2008: Air-sea CO2 flux variability in frontal regions of the Southern Ocean from CARbon Interface OCean Atmosphere drifters. *Limnology and Oceanography*, **53**, 2062–2079, doi:10.4319/lo.2008.53.5_part_2.2062.

Budillon, G., and S. Rintoul, 2003: Fronts and upper ocean thermal variability south of New Zealand. *Antarctic Science*, **15**, 141–152, doi:10.1017/S0954102003001135.

Chapman, C. C., 2014: Southern Ocean jets and how to find them: Improving and comparing common jet detection methods. *Journal of Geophysical Research: Oceans*, **119**, 4318–4339, doi:10.1002/2014JC009810.

582 Close, S. E., A. C. N. Garabato, E. L. Mcdonagh, B. a. King, M. Biuw, and L. Boehme, 2013:
583 Control of Mode and Intermediate Water Mass Properties in Drake Passage by the Amundsen
584 Sea Low. *Journal of Climate*, **26**, 5102–5123, doi:10.1175/JCLI-D-12-00346.1.

585 Cunningham, S., and M. Pavic, 2007: Surface geostrophic currents across the Antarctic Circum-
586 polar Current in Drake Passage from 1992 to 2004. *Progress in Oceanography*, **73**, 296–310,
587 doi:10.1016/j.pocean.2006.07.010.

588 De Boer, A. M., R. M. Graham, M. D. Thomas, and K. E. Kohfeld, 2013: The control of the
589 Southern Hemisphere Westerlies on the position of the Subtropical Front. *Journal of Geophysi-*
590 *cal Research*, **118**, 5669–5675, doi:10.1002/jgrc.20407.

591 Ding, Q., E. J. Steig, D. S. Battisti, and M. Küttel, 2011: Winter warming in West Antarc-
592 tica caused by central tropical Pacific warming. *Nature Geoscience*, **4**, 398–403, doi:10.1038/
593 ngeo1129.

594 Dong, S., J. Sprintall, and S. T. Gille, 2006: Location of the Antarctic Polar Front from AMSR-
595 E Satellite Sea Surface Temperature Measurements. *Journal of Physical Oceanography*, **36**,
596 2075–2089, doi:10.1175/JPO2973.1.

597 Durack, P. J., and S. E. Wijffels, 2010: Fifty-Year Trends in Global Ocean Salinities and
598 Their Relationship to Broad-Scale Warming. *Journal of Climate*, **23**, 4342–4362, doi:10.1175/
599 2010JCLI3377.1.

600 Firing, Y. L., T. K. Chereskin, and M. R. Mazloff, 2011: Vertical structure and transport of the
601 Antarctic Circumpolar Current in Drake Passage from direct velocity observations. *Journal of*
602 *Geophysical Research: Oceans*, **116**, C08 015, doi:10.1029/2011JC006999.

603 Gille, S. T., 1994: Mean sea surface height of the Antarctic Circumpolar Current from Geosat
604 data: Method and application. *Journal of Geophysical Research*, **99**, 18 255–18 273, doi:10.
605 1029/94JC01172.

606 Gille, S. T., 2008: Decadal-Scale Temperature Trends in the Southern Hemisphere Ocean. *Journal*
607 *of Climate*, **21**, 4749–4765, doi:10.1175/2008JCLI2131.1.

608 Gille, S. T., 2014: Meridional displacement of the Antarctic Circumpolar Current. *Philosophical*
609 *transactions. Series A, Mathematical, Physical, and Engineering Sciences*, **372**, 20130 273, doi:
610 10.1098/rsta.2013.0273.

611 Gould, J., and Coauthors, 2004: Argo profiling floats bring new era of in situ ocean observations.
612 *Eos, Transactions American Geophysical Union*, **85**, 185–191, doi:10.1029/2004EO190002.

613 Graham, R. M., A. M. De Boer, K. J. Heywood, M. R. Chapman, and D. P. Stevens, 2012:
614 Southern Ocean fronts: Controlled by wind or topography? *Journal of Geophysical Research:*
615 *Oceans*, **117**, C08 018, doi:10.1029/2012JC007887.

616 Hofmann, D. J., S. Oltmans, J. Harris, B. Johnson, and J. Lathrop, 1997: Ten years of ozonesonde
617 measurements at the south pole: Implications for recovery of springtime Antarctic ozone. *J.*
618 *Geophys. Res.*, **102**, 8931–8943, doi:10.1029/96JD03749.

619 Holland, P. R., and R. Kwok, 2012: Wind-driven trends in Antarctic sea-ice drift. *Nature Geo-*
620 *science*, **5**, 872–875, doi:10.1038/ngeo1627.

621 Ito, T., M. Woloszyn, and M. Mazloff, 2010: Anthropogenic carbon dioxide transport in the South-
622 ern Ocean driven by Ekman flow. *Nature*, **463**, 80–83, doi:10.1038/nature08687.

623 Jacobs, S. S., and C. F. Giulivi, 2010: Large Multidecadal Salinity Trends near the PacificAntarctic
624 Continental Margin. *Journal of Climate*, **23**, 4508–4524, doi:10.1175/2010JCLI3284.1.

Johnson, G. C., 2008: Quantifying Antarctic Bottom Water and North Atlantic Deep Water volumes. *Journal of Geophysical Research*, **113**, C05 027, doi:10.1029/2007JC004477.

Johnson, G. C., S. G. Purkey, and J. L. Bullister, 2008: Warming and Freshening in the Abyssal Southeastern Indian Ocean*. *Journal of Climate*, **21**, 5351–5363, doi:10.1175/2008JCLI2384.1.

Kim, Y. S., and A. H. Orsi, 2014: On the Variability of Antarctic Circumpolar Current Fronts Inferred from 1992-2011 Altimetry*. *Journal of Physical Oceanography*, **44**, 3054–3071, doi:10.1175/JPO-D-13-0217.1.

Klatt, O., O. Boebel, and E. Fahrbach, 2007: A Profiling Float's Sense of Ice. *Journal of Atmospheric and Oceanic Technology*, **24**, 1301–1308, doi:10.1175/JTECH2026.1.

Kobayashi, T., K. Mizuno, and T. Suga, 2012: Long-term variations of surface and intermediate waters in the southern Indian Ocean along 32S. *Journal of Oceanography*, **68**, 243–265, doi:10.1007/s10872-011-0093-5.

Le Quere, C., and Coauthors, 2009: Trends in the sources and sinks of carbon dioxide. *Nature Geoscience*, **2**, 831–836, doi:10.1038/ngeo689.

Lumpkin, R., and K. Speer, 2007: Global Ocean Meridional Overturning. *J. Phys. Oceanogr.*, **37**, 2550–2562, doi:10.1175/JPO3130.1.

Marshall, G. J., 2003: Trends in the Southern Annular Mode from Observations and Reanalyses. *Journal of Climate*, **16**, 4134–4143, doi:10.1175/1520-0442(2003)016⟨4134:TITSAM⟩2.0.CO;2.

Marshall, J., and K. Speer, 2012: Closure of the meridional overturning circulation through Southern Ocean upwelling. *Nature Geoscience*, **5**, 171–180, doi:10.1038/ngeo1391.

Meijers, a. J. S., N. L. Bindoff, and S. R. Rintoul, 2011: Frontal movements and property fluxes: Contributions to heat and freshwater trends in the Southern Ocean. *Journal of Geophysical Research: Oceans*, **116**, C08 024, doi:10.1029/2010JC006832.

Naveira Garabato, A. C., L. Jullion, D. P. Stevens, K. J. Heywood, and B. a. King, 2009: Variability of Subantarctic Mode Water and Antarctic Intermediate Water in the Drake Passage during the Late-Twentieth and Early-Twenty-First Centuries. *Journal of Climate*, **22**, 3661–3688, doi:10.1175/2009JCLI2621.1.

Orsi, A. H., T. Whitworth, and W. D. Nowlin, 1995: On the meridional extent and fronts of the Antarctic Circumpolar Current. *Deep Sea Research Part I: Oceanographic Research Papers*, **42**, 641–673, doi:10.1016/0967-0637(95)00021-W.

Paolo, F. S., H. A. Fricker, and L. Padman, 2015: Volume loss from Antarctic ice shelves is accelerating. *Science*, **348**, 327–331, doi:10.1126/science.aaa0940.

Park, Y.-H., I. Durand, E. Kestenare, G. Rougier, M. Zhou, F. D'Ovidio, C. Cotté, and J.-H. Lee, 2014: Polar Front around the Kerguelen Islands: An up-to-date determination and associated circulation of surface/subsurface waters. *Journal of Geophysical Research: Oceans*, **119**, 6575–6592, doi:10.1002/2014JC010061.

Park, Y.-H., F. Vivier, F. Roquet, and E. Kestenare, 2009: Direct observations of the ACC transport across the Kerguelen Plateau. *Geophysical Research Letters*, **36**, L18 603, doi:10.1029/2009GL039617.

Peterson, R. G., and T. Whitworth, 1989: The subantarctic and polar fronts in relation to deep water masses through the southwestern Atlantic. *Journal of Geophysical Research*, **94**, 10 817–10 838, doi:10.1029/JC094iC08p10817.

668 Purkey, S. G., and G. C. Johnson, 2010: Warming of Global Abyssal and Deep Southern Ocean
669 Waters between the 1990s and 2000s: Contributions to Global Heat and Sea Level Rise Bud-
670 gets*. *Journal of Climate*, **23**, 6336–6351, doi:10.1175/2010JCLI3682.1.

671 Purkey, S. G., and G. C. Johnson, 2013: Antarctic Bottom Water Warming and Freshening: Con-
672 tributions to Sea Level Rise, Ocean Freshwater Budgets, and Global Heat Gain. *Journal of*
673 *Climate*, **26**, 6105–6122, doi:10.1175/JCLI-D-12-00834.1.

674 Renault, A., C. Provost, N. Sennéchael, N. Barré, and A. Kartavtseff, 2011: Two full-depth ve-
675 locity sections in the Drake Passage in 2006 - Transport estimates. *Deep-Sea Research Part II:*
676 *Topical Studies in Oceanography*, **58**, 2572–2591, doi:10.1016/j.dsr2.2011.01.004.

677 Rignot, E., S. Jacobs, J. Mouginot, and B. Scheuchl, 2013: Ice-Shelf Melting Around Antarctica.
678 *Science*, **341**, 266–270, doi:10.1126/science.1235798.

679 Rignot, E., J. Mouginot, M. Morlighem, H. Seroussi, and B. Scheuchl, 2014: Widespread,
680 rapid grounding line retreat of Pine Island, Thwaites, Smith, and Kohler glaciers, West
681 Antarctica, from 1992 to 2011. *Geophysical Research Letters*, **41**, 3502–3509, doi:10.1002/
682 2014GL060140.

683 Rintoul, S. R., C. Hughes, and D. Olbers, 2001: *Ocean Circulation and Climate - The Antarctic*
684 *Circumpolar System*, chap. 4.6, 271–302. Academic Press.

685 Roemmich, D., J. Church, J. Gilson, D. Monselesan, P. Sutton, and S. Wijffels, 2015: Unabated
686 planetary warming and its ocean structure since 2006. *Nature Clim. Change*, **5**, 240–245, doi:
687 10.1038/nclimate2513.

688 Roemmich, D., and J. Gilson, 2009: The 2004-2008 mean and annual cycle of temperature, salin-
689 ity, and steric height in the global ocean from the Argo Program. *Progress in Oceanography*,
690 **82**, 81–100, doi:10.1016/j.pocean.2009.03.004.

691 Roemmich, D., and Coauthors, 2009: The Argo Program: Observing the Global Oceans with
692 Profiling Floats. *Oceanography*, **22**, 34–43, doi:10.5670/oceanog.2009.36.

693 Sabine, C. L., 2004: The Oceanic Sink for Anthropogenic CO2. *Science*, **305**, 367–371, doi:
694 10.1126/science.1097403.

695 Sallee, J.-B., R. J. Matear, S. R. Rintoul, and A. Lenton, 2012: Localized subduction of anthro-
696 pogenic carbon dioxide in the Southern Hemisphere oceans. *Nature Geoscience*, **5**, 579–584,
697 doi:10.1038/ngeo1523.

698 Sallée, J. B., K. Speer, and R. Morrow, 2008: Response of the Antarctic Circumpolar Current to
699 Atmospheric Variability. *Journal of Climate*, **21**, 3020–3039, doi:10.1175/2007JCLI1702.1.

700 Schmidtko, S., K. J. Heywood, A. F. Thompson, and S. Aoki, 2014: Multidecadal warming of
701 Antarctic waters. *Science*, **346**, 1227–1231, doi:10.1126/science.1256117.

702 Schmidtko, S., and G. C. Johnson, 2012: Multidecadal Warming and Shoaling of Antarctic Inter-
703 mediate Water*. *Journal of Climate*, **25**, 207–221, doi:10.1175/JCLI-D-11-00021.1.

704 Shao, A. E., S. T. Gille, S. Mecking, and L. Thompson, 2015: Properties of the Subantarctic Front
705 and Polar Front from the skewness of sea level anomaly. *Journal of Geophysical Research:*
706 *Oceans*, **120**, 5179–5193, doi:10.1002/2015JC010723.

707 Sokolov, S., and S. R. Rintoul, 2002: Structure of Southern Ocean fronts at 140E. *Journal of*
708 *Marine Systems*, **37**, 151–184, doi:10.1016/S0924-7963(02)00200-2.

709 Sokolov, S., and S. R. Rintoul, 2007: Multiple Jets of the Antarctic Circumpolar Current South of
710 Australia*. *Journal of Physical Oceanography*, **37**, 1394–1412, doi:10.1175/JPO3111.1.

711 Sokolov, S., and S. R. Rintoul, 2009a: Circumpolar structure and distribution of the Antarctic
712 Circumpolar Current fronts: 1. Mean circumpolar paths. *Journal of Geophysical Research:*
713 *Oceans*, **114**, C11 018, doi:10.1029/2008JC005108.

714 Sokolov, S., and S. R. Rintoul, 2009b: Circumpolar structure and distribution of the Antarctic
715 Circumpolar Current fronts: 2. Variability and relationship to sea surface height. *Journal of*
716 *Geophysical Research: Oceans*, **114**, C11 019, doi:10.1029/2008JC005248.

717 Sparrow, M. M., K. K. Heywood, J. Brown, and D. Stevens, 1996: Current structure of
718 the south Indian Ocean. *Journal of Geophysical Research: Oceans*, **101**, 6377–6391, doi:
719 10.1029/95JC03750.

720 Sprintall, J., 2008: Long-term trends and interannual variability of temperature in Drake Passage.
721 *Progress in Oceanography*, **77**, 316–330, doi:10.1016/j.pocean.2006.06.004.

722 Sutton, P., and D. Roemmich, 2011: Decadal steric and sea surface height changes in the Southern
723 Hemisphere. *Geophysical Research Letters*, **38**, L08 604, doi:10.1029/2011GL046802.

724 Swart, S., and S. Speich, 2010: An altimetry-based gravest empirical mode south of Africa: 2.
725 Dynamic nature of the Antarctic circumpolar current fronts. *Journal of Geophysical Research:*
726 *Oceans*, **115**, C03 003, doi:10.1029/2009JC005300.

727 Tarakanov, R. Y., 2011: Southern Jets of the Antarctic Circumpolar Current in the Eastern Pacific
728 Antarctic. *Oceanology*, **51**, 588–598, doi:10.1134/S0001437011040175.

729 Tarakanov, R. Y., 2014: Jets of the Antarctic Circumpolar Current in the Central Part of the Drake
730 Passage Based on the Survey Data in October-November of 2008. *Oceanology*, **54**, 1–7, doi:
731 10.1134/S000143701401010X.

732 Thompson, A. F., P. H. Haynes, C. Wilson, and K. J. Richards, 2010: Rapid Southern Ocean
733 front transitions in an eddy-resolving ocean GCM. *Geophysical Research Letters*, **37**, L23 602,
734 doi:10.1029/2010GL045386.

735 Thompson, A. F., and J.-B. Sallee, 2012: Jets and Topography: Jet Transitions and the Impact on
736 Transport in the Antarctic Circumpolar Current. *Journal of Physical Oceanography*, **42**, 956–
737 972, doi:10.1175/JPO-D-11-0135.1.

738 Thompson, D. W. J., S. Solomon, P. J. Kushner, M. H. England, K. M. Grise, and D. J. Karoly,
739 2011: Signatures of the Antarctic ozone hole in Southern Hemisphere surface climate change.
740 *Nature Geoscience*, **4**, 741–749, doi:10.1038/ngeo1296.

741 Thompson, K. R., and E. Demirov, 2006: Skewness of sea level variability of the world's oceans.
742 *Journal of Geophysical Research: Oceans*, **111**, C05 005, doi:10.1029/2004JC002839.

743 Van Sebille, E., P. Spence, M. R. Mazloff, M. H. England, S. R. Rintoul, and O. a. Saenko,
744 2013: Abyssal connections of Antarctic Bottom Water in a Southern Ocean State Estimate.
745 *Geophysical Research Letters*, **40**, 2177–2182, doi:10.1002/grl.50483.

746 Watson, A. J., M. P. Meredith, and J. C. Marshall, 2014: The Southern Ocean, carbon and climate.
747 *Philosophical transactions. Series A, Mathematical, Physical, and Engineering Sciences*, **372**,
748 20130 057, doi:10.1098/rsta.2013.0057.

749 WMO, 2011: Scientific Assessment of Ozone Depletion. Global Ozone Research and Monitoring,
750 Project Report No. 52.

751 Yang, X. Y., and Z. He, 2014: Decadal change of Antarctic Intermediate Water in the region of
752 Brazil and Malvinas confluence. *Deep-Sea Research Part I: Oceanographic Research Papers*,
753 **88**, 1–7, doi:10.1016/j.dsr.2014.02.007.

LIST OF TABLES

TABLE 1. Time mean θ^* (°C) from this study (i.e. along the DH-based ACC fronts from the gridded Argo data, Fig. 3), Orsi et al. (1995) (OWN95), and Sokolov and Rintoul (2009a) (SR09, their Table 1). Values for both the middle and northern branch of the SAf in SR09 are in the nSAf column. The standard deviation ($\pm 1\sigma$) along the front is also indicated, as well as water masses related to each criterion (UCDW is Upper Circumpolar Deep Water).

	Pf		**sSAf**	**nSAf**
	min(θ) at p$\leq$200 dbar	**max(θ) at p$\geq$800 dbar**	**θ at p=400 dbar**	
this study	1.3±0.41	2.17±0.06	3.34±0.35	5.05±0.63
OWN95	2	2.2	4	5
SR09	1.15±0.16	2.25±0.07	2.78±0.15	4.06±0.35, 6.06±0.79
	Winter Water dives northward, θ_{min}	UCDW shoals southward (θ_{max}) or just θ at 800 dbar	colder ACC vs warmer subtropics	

LIST OF FIGURES

(a) and (b)). In panel (a), dashed lines coincide with dotted ones, since θ^* values are from OWN95. In panel (b), dashed lines are for θ^* computed along DH-based fronts. Dot colors represent mean pressure (dbar) at the θ-S values along the fronts. 46

Fig. 8. Yearly θ-S diagram along the Argo (a) nSAf and (b) Pf in Fig. 3. Errorbars are shown around each dot. Gray contours indicate isopycnals. The 200, 400, 600 dbar pressure levels are marked, with pressure increasing from warmer to colder for the nSAf and from fresher to saltier for the Pf. 47

Fig. 9. Yearly (left) heat and (right) freshwater content anomalies from the 2006−2013 time mean, in different regions of the SO (legend in panel b, and maps in Fig. 2b) and for different pressure ranges (tops and bottoms of pressure layers are indicated in the title). Dots signify that the yearly value is larger than its standard error. Freshwater values are in cm, after normalizing the volume of freshwater by the area of the SO within the Argo domain ($6.001 \cdot 10^{13}$ m^2). The legend in the left panels indicates the ocean volume in each region. 48

Fig. 10. Maps of yearly freshwater content (m) anomalies from the 2006−2013 time mean, for the $0-1975$ dbar pressure range, with zero contour (thin black line). Black dots signify that the yearly value is smaller than its standard error. DH-based Argo fronts are indicated as thick lines as in Fig. 2b. 49

Fig. 11. Yearly (top) heat and (bottom) freshwater content anomalies from the 2006−2013 time mean in different regions of the SO (same regions as in Fig. 9) and in 0.05 kg m^{-3} thick potential density classes (y-axis). Values are based on the time mean location of isopycnals. Freshwater values follow Fig. 9. Black contours: pressure on isopycnals. Years since 2000 are indicated on the x-axis. 50

Fig. 12. Yearly anomalies from the 2006−2013 time mean of (top) potential temperature, (middle) salinity, and (bottom) potential density on the mean locations of a set of isopycnals (y-axis, kg m^{-3}). Regions follow Fig. 9. Black contours: pressure on isopycnals. Years since 2000 are indicated on the x-axis. 51

Fig. 13. Following Fig. 12, but on the actual (time varying) isopycnal locations. Bottom panels show pressure anomalies on isopycnals. 52

Fig. 14. Comparison of pressure changes on isopycnals (a) estimated from ECMWF ERA-Interim wind stress curl (i.e. Ekman upwelling and downwelling), and (b-d) observed by Argo in different regions (following Fig. 9). Changes are indicated as the cumulative sum of monthly dp (i.e. difference in pressure between month i and month i-1) since the beginning of 2006 (to the end of the year in the x-axis). In panels (b-d), light to dark shades are for lighter to denser isopycnals. Also, in panels (b-d), dashed lines indicate the estimate from Ekman upwelling and downwelling shown in panel (a). 53

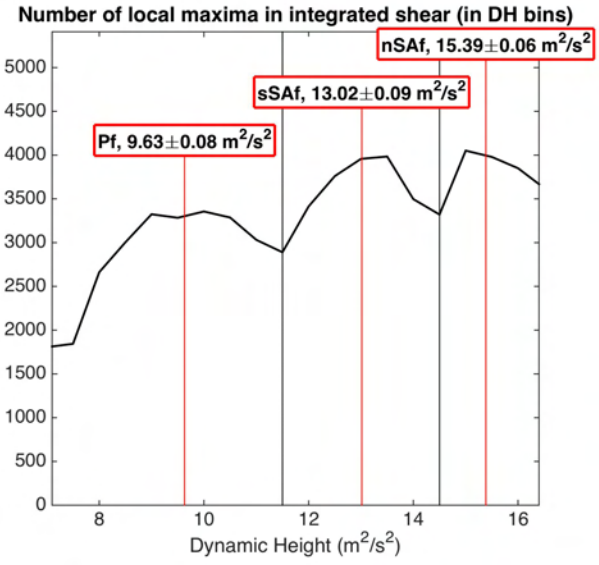

FIG. 1. Number of local maxima in vertically integrated geostrophic shear ($0-1975$ dbar) from gridded Argo data, considering all longitudes, latitudes (south of 35.5°S), and months from 2006-2013, binned by Dynamic Height (DH). Gray lines separate DH ranges encompassing different fronts. Red lines indicate the DH contour assigned to each front (values and standard errors in red boxes, along with abbreviations for the fronts).

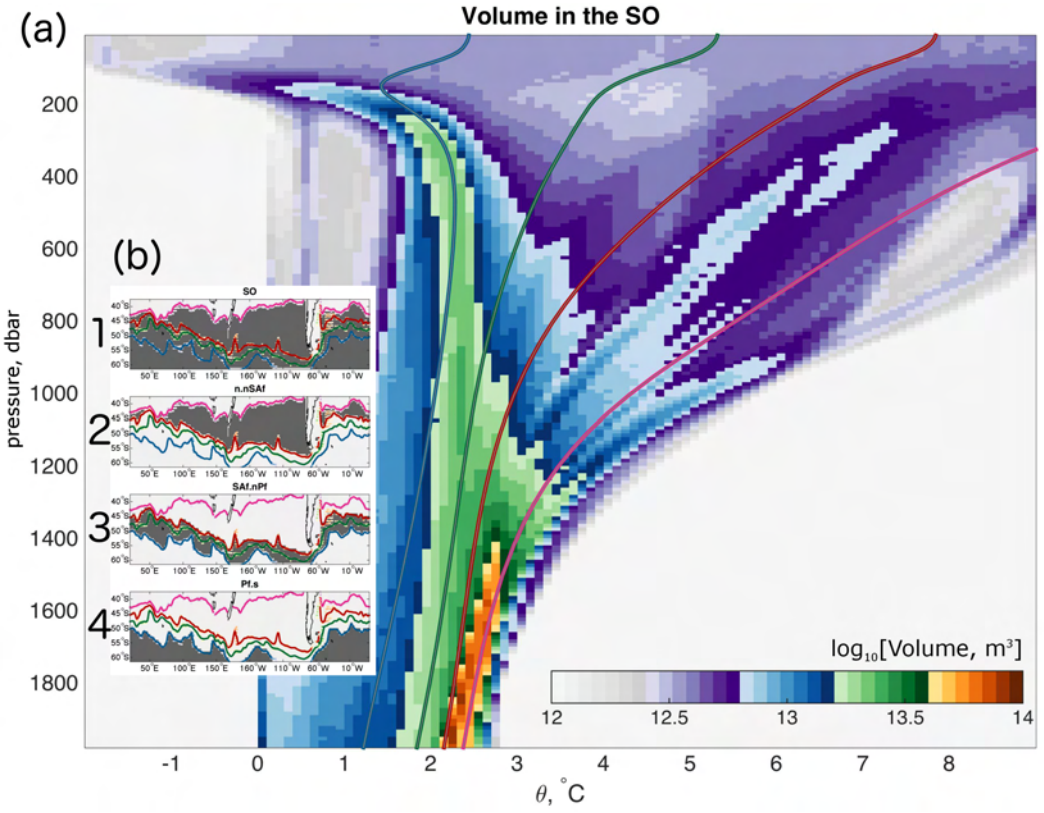

FIG. 2. (a) Time mean volume in θ (x-axis, °C) and pressure (y-axis, dbar) bins, within the Argo domain south of the Subtropical Front (STf), i.e. gray shaded region in panel b1. The volume in each bin (m^3) is equal to 10 power of the value shaded in color. The mean θ profiles along the DH-based Argo fronts in Fig. 3 (and along the STf) are indicated as thick lines (Pf in blue, sSAf in green, nSAf in red, STf in magenta). (b) Regions of the Argo domain, considered in this study, are shaded gray: (b1) SO (south of the STf), (b2) n.nSAf (between the STf and the nSAf), (b3) SAf.nPf (nSAf to north of the Pf), and (b4) Pf.s (Pf and south). The time mean location of the Argo fronts is color coded as in panel (a).

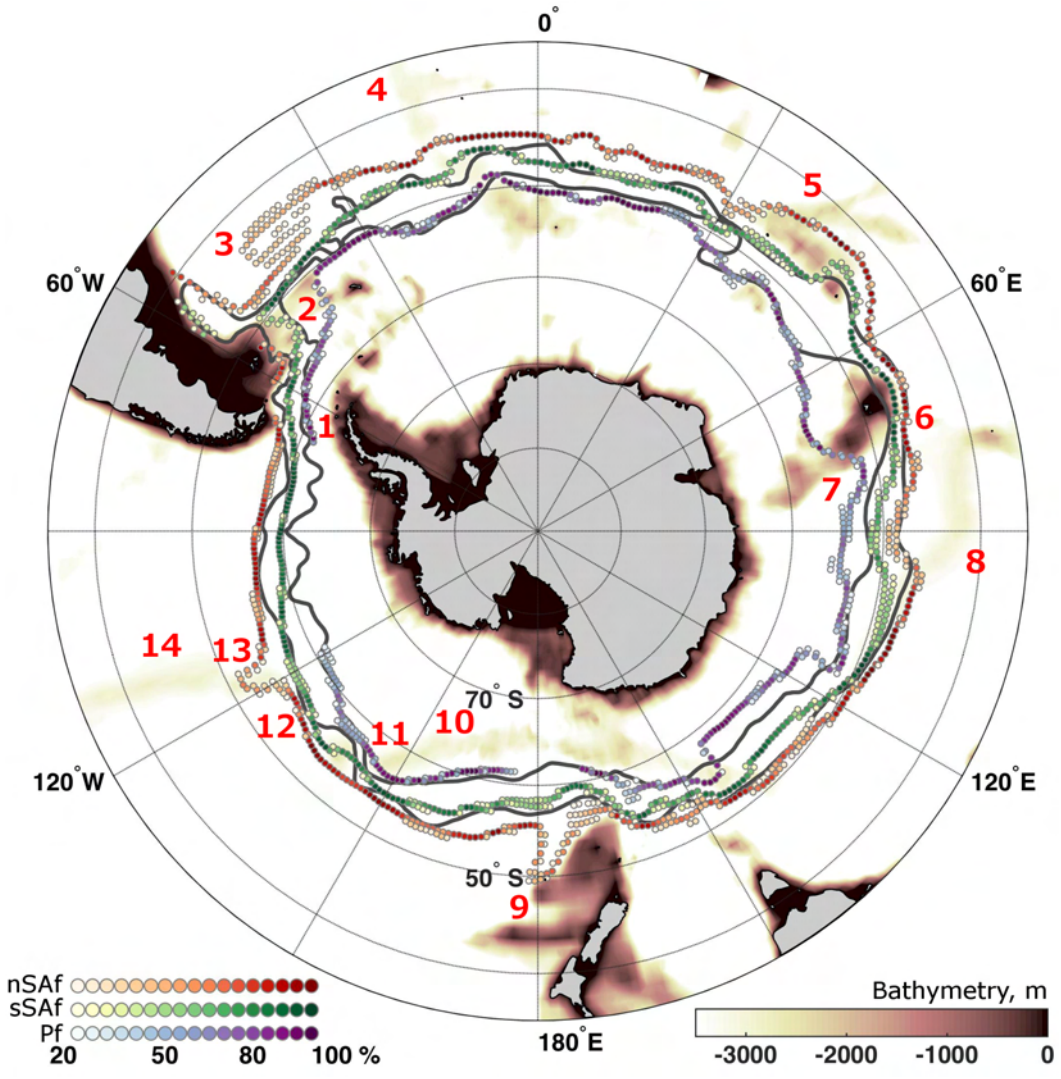

FIG. 3. DH-based ACC fronts from gridded Argo data: frequency of occurrence (dots) during 2006 – 2013 (values smaller than 20% are masked out). Light blue to purple dots are for the Polar Front (Pf). Light yellow to green dots are for the Southern Subantarctic Front (sSAf). Light Orange to red dots are for the Northern Subantarctic Front (nSAf). Black lines are, from north to south, the Subantarctic and Polar fronts described in Orsi et al. (1995) (OWN95). Bathymetry (m) shallower than 3500 m is shaded from white to dark brown, in the background. Numbers (in red) are adjacent to some of the main bathymetric features: (1) Drake Passage, (2) Maurice Ewing Bank, (3) Argentine Basin, (4) Atlantic Ridge, (5) SW Indian Ridge, (6) Kerguelen Plateau, (7) Fawn Trough, (8) SE Indian Ridge, (9) Campbell Plateau, (10) Pacific-Antarctic Ridge, (11) Udintsev Fracture Zone, (12) Eltanin Fracture Zone, (13) Menard Fracture Zone, and (14) East Pacific Rise.

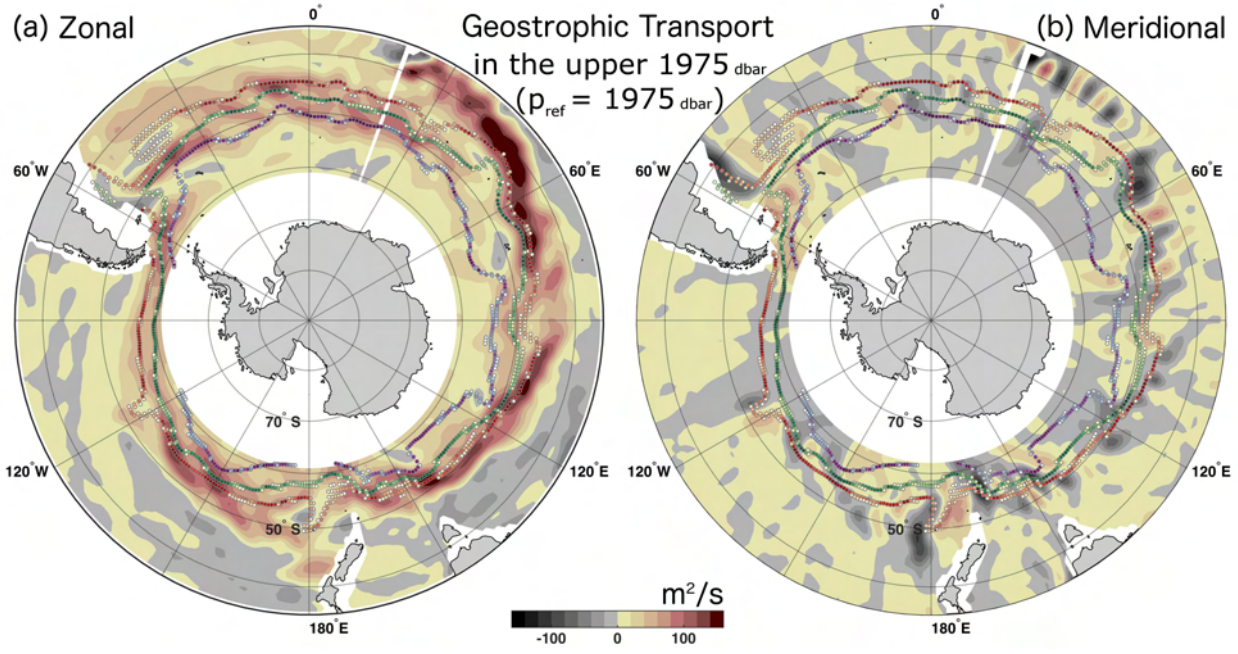

867 FIG. 4. DH-based Argo fronts as in Fig. 3, with the background color showing the time mean (a) zonal and
868 (b) meridional baroclinic geostrophic transport per unit meter ($m^2 s^{-1}$), in the upper 1975 dbar, from gridded
869 Argo data.

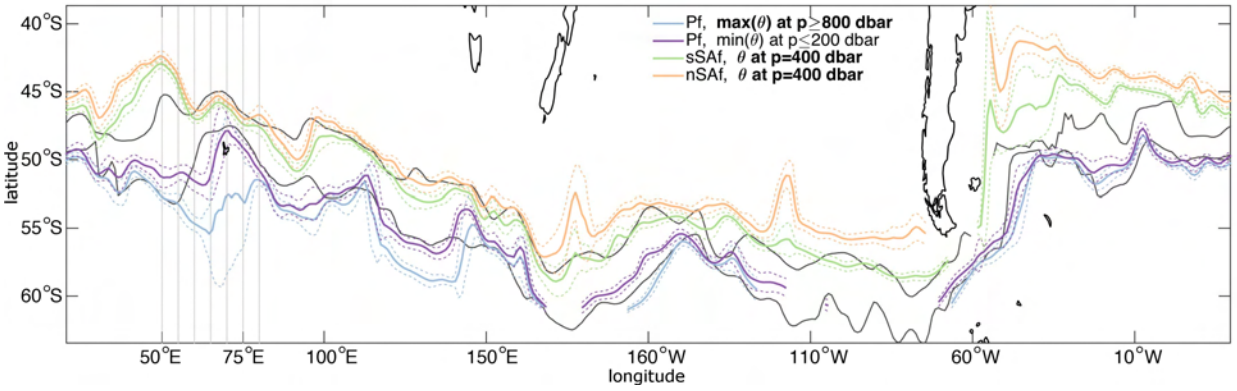

FIG. 5. Argo fronts from θ-criteria (thick lines), using θ^* values consistent with OWN95 (Table 1): x,y locations are averaged in 1 degree longitude bins and in time. Errorbars (dashed lines) include a component related to the bin average and another equal to 1 (temporal) standard deviation of the front meridional location. Bold fonts highlight, in the legend, θ criteria that align best with DH-based fronts. Polar and Subantarctic fronts from OWN95 are shown as black lines. A 5 degree grid is added along the x-axis between $50-80°$E.

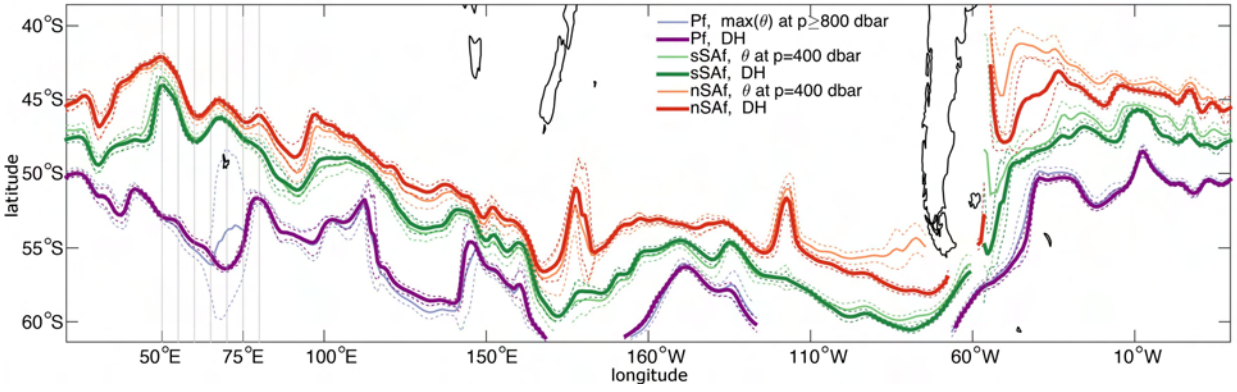

875 FIG. 6. DH-based (thick lines) and θ-based (thin lines) Argo fronts (with θ^* values computed along the
876 DH-based fronts, Table 1): x,y locations are averaged in 1 degree longitude bins and in time. Errorbars (dashed
877 lines), include a component related to the bin average and another equal to 1 (temporal) standard deviation of
878 the front meridional location. A 5 degree grid is added along the x-axis between $50-80^{\circ}$E.

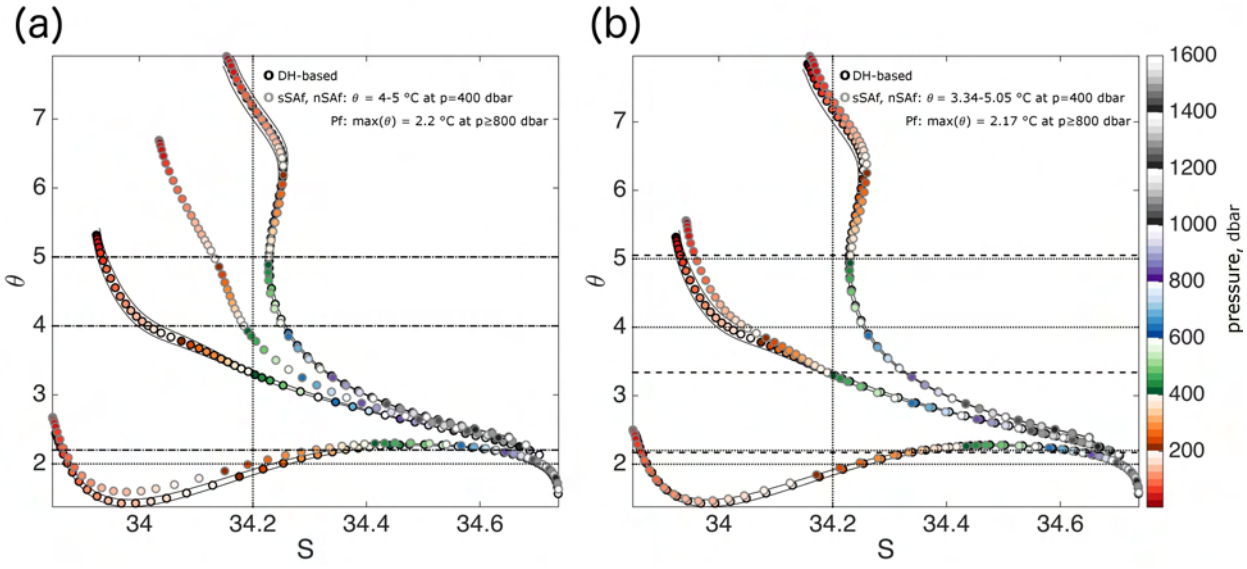

879 FIG. 7. Comparison of time mean θ-S diagrams along the DH-based Argo fronts in Fig. 3 (black edge dots in
880 panel (a) and (b)), with those from the θ-based Argo fronts (in bold) in Fig. 5 (gray edge dots in panel (a)), and
881 in Fig. 6 (gray edge dots in panel (b)), with θ from colder to warmer along the Pf, sSAf, and nSAf. Errorbars
882 (black solid lines) are indicated for the DH-based fronts, consistent with the error on the DH contour choice
883 associated with each front (Fig. 1). In both panels, dotted lines indicate θ^*-S* values described in OWN95.
884 Dashed lines indicate θ^* values used to locate the θ-based fronts (different between panel (a) and (b)). In panel
885 (a), dashed lines coincide with dotted ones, since θ^* values are from OWN95. In panel (b), dashed lines are
886 for θ^* computed along DH-based fronts. Dot colors represent mean pressure (dbar) at the θ-S values along the
887 fronts.

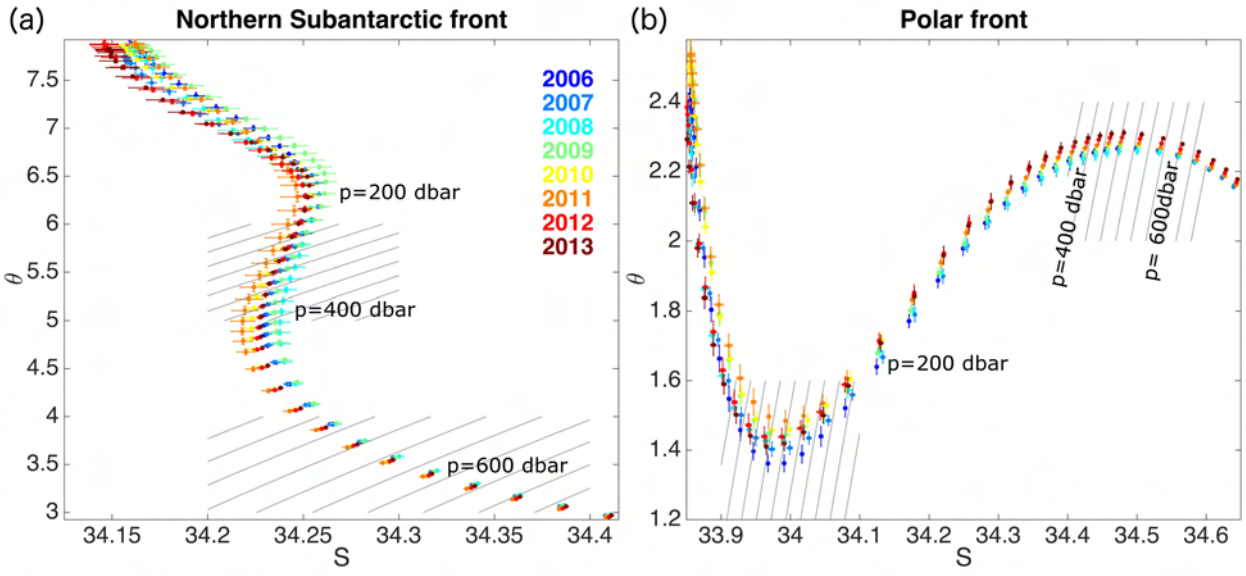

888 FIG. 8. Yearly θ-S diagram along the Argo (a) nSAf and (b) Pf in Fig. 3. Errorbars are shown around each dot.
889 Gray contours indicate isopycnals. The 200, 400, 600 dbar pressure levels are marked, with pressure increasing
890 from warmer to colder for the nSAf and from fresher to saltier for the Pf.

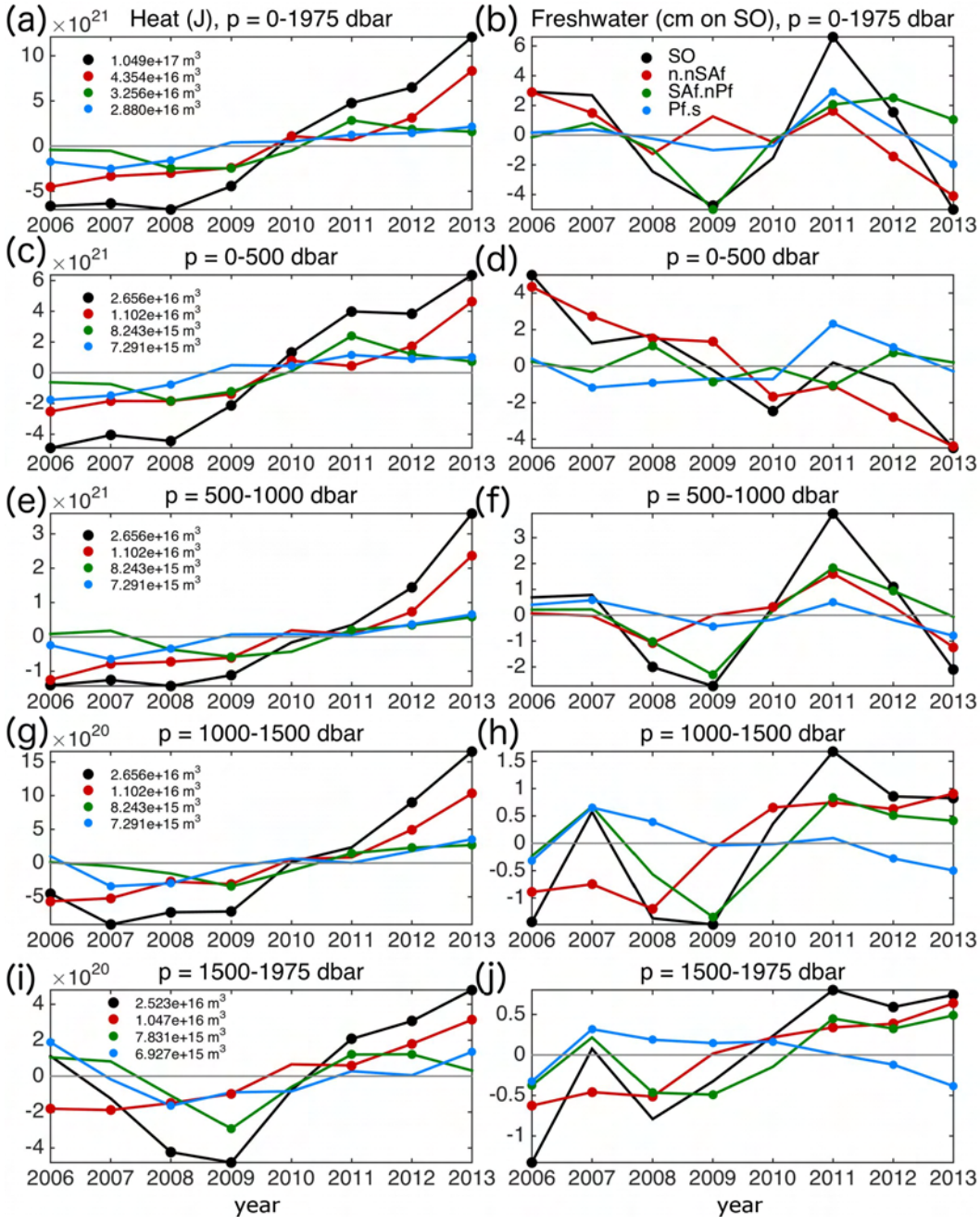

FIG. 9. Yearly (left) heat and (right) freshwater content anomalies from the 2006−2013 time mean, in different regions of the SO (legend in panel b, and maps in Fig. 2b) and for different pressure ranges (tops and bottoms of pressure layers are indicated in the title). Dots signify that the yearly value is larger than its standard error. Freshwater values are in cm, after normalizing the volume of freshwater by the area of the SO within the Argo domain ($6.001 \cdot 10^{13}$ m^2). The legend in the left panels indicates the ocean volume in each region.

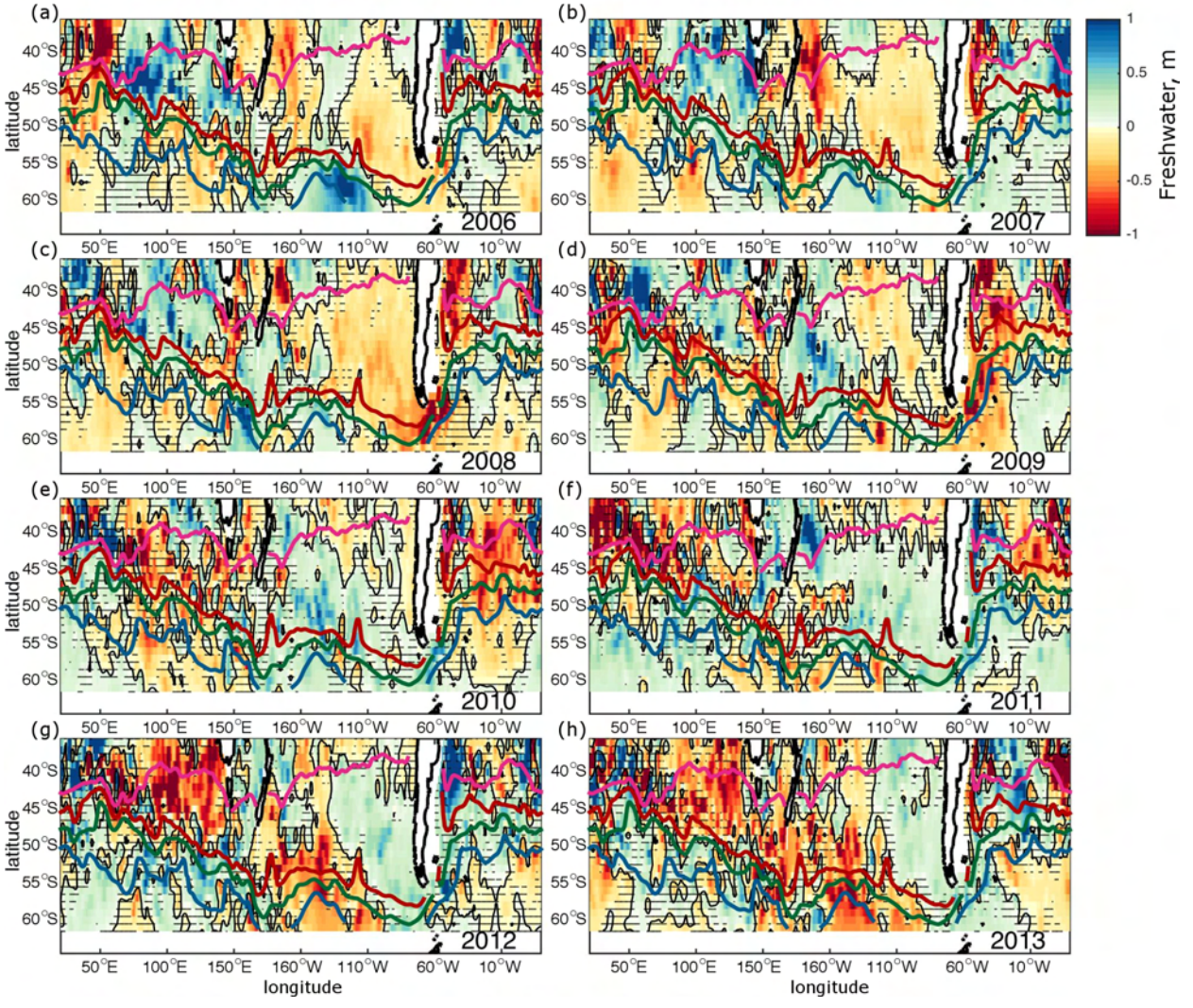

FIG. 10. Maps of yearly freshwater content (m) anomalies from the 2006−2013 time mean, for the 0 – 1975 dbar pressure range, with zero contour (thin black line). Black dots signify that the yearly value is smaller than its standard error. DH-based Argo fronts are indicated as thick lines as in Fig. 2b.

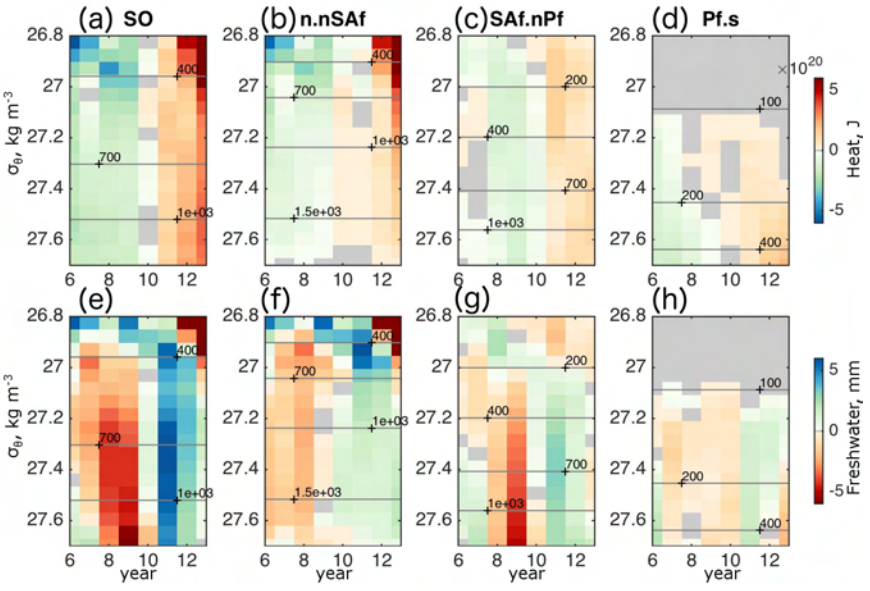

FIG. 11. Yearly (top) heat and (bottom) freshwater content anomalies from the 2006−2013 time mean in different regions of the SO (same regions as in Fig. 9) and in 0.05 $\mathrm{kg\,m^{-3}}$ thick potential density classes (y-axis). Values are based on the time mean location of isopycnals. Freshwater values follow Fig. 9. Black contours: pressure on isopycnals. Years since 2000 are indicated on the x-axis.

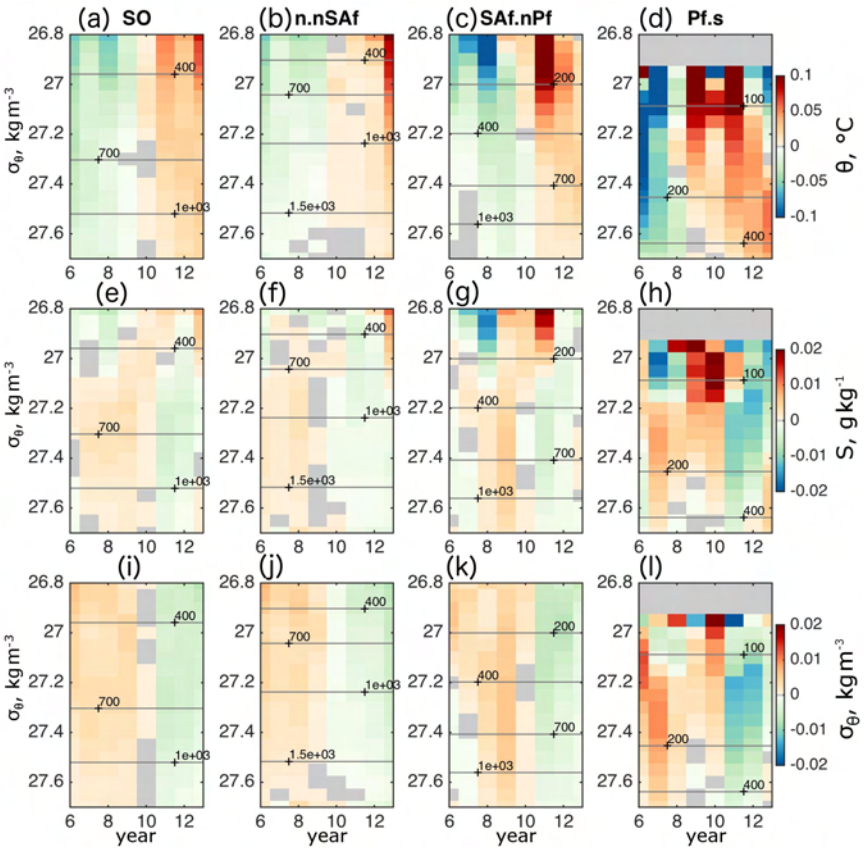

FIG. 12. Yearly anomalies from the 2006−2013 time mean of (top) potential temperature, (middle) salinity, and (bottom) potential density on the mean locations of a set of isopycnals (y-axis, $\mathrm{kg\,m^{-3}}$). Regions follow Fig. 9. Black contours: pressure on isopycnals. Years since 2000 are indicated on the x-axis.

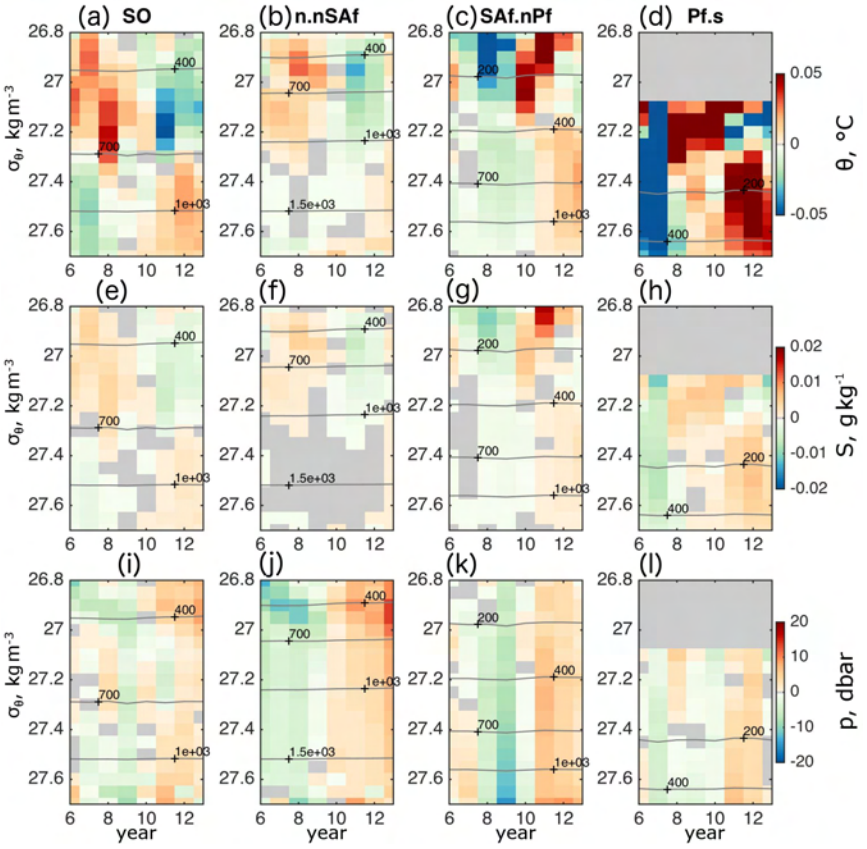

906 FIG. 13. Following Fig. 12, but on the actual (time varying) isopycnal locations. Bottom panels show pressure
907 anomalies on isopycnals.

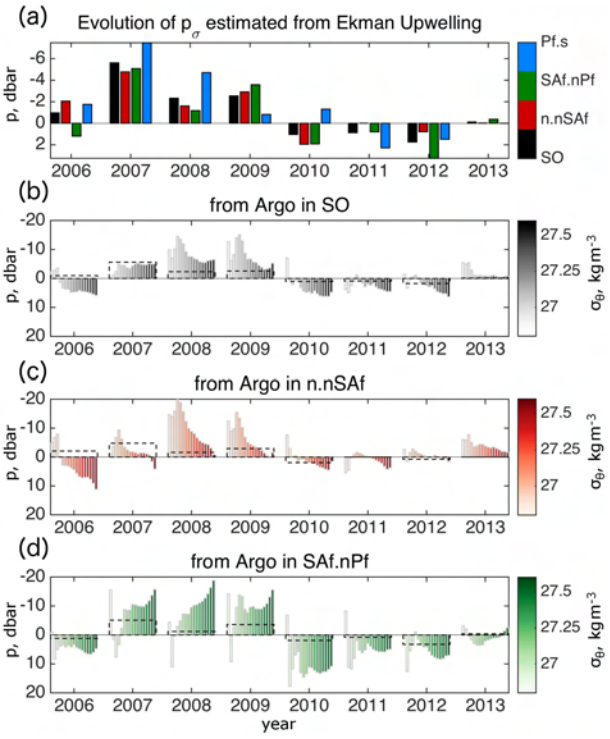

908 FIG. 14. Comparison of pressure changes on isopycnals (a) estimated from ECMWF ERA-Interim wind stress
909 curl (i.e. Ekman upwelling and downwelling), and (b-d) observed by Argo in different regions (following Fig.
910 9). Changes are indicated as the cumulative sum of monthly dp (i.e. difference in pressure between month i
911 and month i-1) since the beginning of 2006 (to the end of the year in the x-axis). In panels (b-d), light to dark
912 shades are for lighter to denser isopycnals. Also, in panels (b-d), dashed lines indicate the estimate from Ekman
913 upwelling and downwelling shown in panel (a).